



Impact of the acquisition protocol on the sensitivity to demyelination and axonal loss of clinically feasible DWI techniques: a simulation study

Stefania Oliviero¹ · Cosimo Del Gratta¹

Received: 6 July 2020 / Revised: 19 November 2020 / Accepted: 22 November 2020 / Published online: 8 January 2021
© European Society for Magnetic Resonance in Medicine and Biology (ESMRMB) 2021

Abstract

Objective To evaluate: (a) the specific effect that the demyelination and axonal loss have on the DW signal, and (b) the impact of the sequence parameters on the sensitivity to damage of two clinically feasible DWI techniques, i.e. DKI and NODDI.

Methods We performed a Monte Carlo simulation of water diffusion inside a novel synthetic model of white matter in the presence of axonal loss and demyelination, with three compartments with permeable boundaries between them. We compared DKI and NODDI in their ability to detect and assess the damage, using several acquisition protocols. We used the *F* test statistic as an index of the sensitivity for each DWI parameter to axonal loss and demyelination, respectively.

Results DKI parameters significantly changed with increasing axonal loss, but, in most cases, not with demyelination; all the NODDI parameters showed sensitivity to both the damage processes (at $p < 0.01$). However, the acquisition protocol strongly affected the sensitivity to damage of both the DKI and NODDI parameters and, especially for NODDI, the parameter absolute values also.

Discussion This work is expected to impact future choices for investigating white matter microstructure in focusing on specific stages of the disease, and for selecting the appropriate experimental framework to obtain optimal data quality given the purpose of the experiment.

Keywords Axonal loss · Demyelination · DKI · NODDI · Monte carlo diffusion simulation · *g*-ratio

Introduction

Diffusion-weighted imaging (DWI) is a powerful non-invasive imaging technique that has shown high sensitivity in revealing microstructural changes in damaged brain tissues [1–6]. DWI provides valuable information about tissue microstructure by revealing the diffusion motion of water molecules within biological tissue [7–12]. Diffusion movements are hindered, or restricted by cell membranes, organelles, etc., thus, their average cumulants of displacement in time are linked to a diffusion coefficient *D* and depend on the tissue microstructure. DWI methods (e.g. DTI [9], DKI [13], and NODDI [14]) model the

diffusivity inside the tissue and, for a given attenuation of the diffusion-weighted signal, allow to extract *D* and some other parameters reflecting microstructural features of the biological tissues, such as the DTI-derived apparent diffusivity coefficients (MD, AD, RD) [15], the fiber orientation [14, 16–18], and the cell density [14, 16–18]. When pathology affects the central nervous system (CNS), microstructural features may be altered by damage processes such as demyelination or axonal loss, several of which may occur together. Evaluating the impact of each kind of structural change on the DW signal and the DWI parameters is challenging. Specifically, the choice of the acquisition sequence to employ is extremely important because it could significantly affect the accuracy, precision, and sensitivity to the damage of the measured DWI parameters. Greater sensitivity to the damage can potentially uncover the first changes in the lesioned tissues and subtle differences due to the damage progression, invisible to T1 and T2 contrasts. Also, to improve performance, an optimal scheme can reduce acquisition times, which is

✉ Stefania Oliviero
stefania.oliviero@hotmail.it

¹ Department Neurosciences, Imaging, and Clinical Sciences, Institute for Advanced Biomedical Technologies, ITAB, Gabriele D’Annunzio University, Chieti, Italy

essential to ensure the feasibility of advanced DWI methods in clinical studies and, ultimately, to promote their inclusion in the clinical routine. However, optimizing DWI parameters is highly complex, thus, not many studies have proposed optimal experimental designs for multi-shell techniques, and all these studies only considered healthy tissue [14, 19–22]. Also, a few studies [23, 24] have compared different DWI methods (NODDI, DKI, and DTI) in their ability to highlight the same tissue microstructural abnormalities, in multiple sclerosis (MS) in particular.

As a consequence, there is a general lack of agreed-upon guidelines regarding the sequence to use for each specific DWI multi-shell technique, in particular, to optimize the microstructural characterization of lesioned tissues. The purpose of this simulation study is to explore, for the first time, the impact of the acquisition sequence on the ability of two clinically feasible multi-shell DWI techniques (DKI and NODDI) to reveal two specific damage processes typical of many neurological diseases [25–28], i.e. demyelination and axonal loss. Moreover, our study assesses the effect of these tissue damages on the diffusion parameters and compares DKI and NODDI in their capability to characterize a lesion in a given allocated time. In this regard, Monte Carlo simulation of water diffusion is a versatile and powerful technique enabling in silico comparison, design of DWI techniques, and assessment of the sensitivity, specificity, accuracy, and precision of DWI parameters compared to ground truth features, whereas this is difficult or long to perform experimentally.

Specifically, we developed a new white matter WM model including myelinated and permeable axons in the presence of demyelination and axonal loss: our model encompasses some significant novelty elements compared to those previously proposed in the literature [29–37]. In particular, boundary permeability was never considered before, neither in works approaching the damaged conditions of WM [32, 35–37] nor in studies on DWI method validation using computational phantoms (e.g. [14, 18]). However, the effects of cell membrane permeability and water exchange on the diffusion signal are non-negligible when using sequences with diffusion times greater than 12 ms for a healthy brain, and 4 ms for injured conditions [38], but the typical sequences employed in the clinical studies to perform DTI, DKI, or NODDI analysis have diffusion times of about 30–40 ms. In addition to boundary permeability, among the novelty elements is the presence of myelin, characterized by a physiologically plausible relaxation time T_2 [64]. And finally, we introduce new features in modeling demyelination and axonal loss, namely, we consider, for the first time, that the probability of water molecules crossing the myelin sheath depends on the sheath thickness, and that extra-axonal diffusivity is affected by axonal debris occurring together with axonal loss.

Thus, we performed a Monte Carlo simulation of water diffusion motion inside 21 synthetic voxels of WM with the above features (called substrates), and with different degrees of damage; we, then, calculated the DW signal from each substrate with various acquisition protocols. For each DWI method and acquisition sequence, we extracted the parameter values and quantified the parameter sensitivities to the damage processes by using the F test statistic. All the parameter sensitivities were compared with those of DTI, the latter representing the only standard in the current clinical practice. The ultimate goal of this study was to identify a biomarker for demyelinating diseases, using a clinically feasible protocol. We, therefore, tested only protocols with a limited acquisition time (< 30 min) and a limited intensity of the field gradient (< 87 mT/m). Among the DWI methods, we selected DKI and NODDI, since they are widely used to characterize real lesioned tissue in the presence of demyelination and axonal loss [39–53]. They work well with clinically feasible acquisition protocols with the aforementioned constraints and their analysis is easily implementable in the standard clinical practice.

The paper is organized as follows. The Methods section includes two subsections: “Synthetic tissue and Monte Carlo simulation” describing the structural features of the intact and damaged WM model, and “Experimental design” providing details about the study design, and the acquisition protocols selected for each DWI method. The Results section shows the specific effect that the demyelination and axonal loss have on the DTI, DKI, and NODDI parameters; it demonstrates how the acquisition protocol strongly impacts the parameter sensitivity and, finally, compares the methods in their ability to reveal the damage, for a given allocated time. Finally, the Discussion section reports on the implications of the findings.

Materials and methods

Synthetic tissue and Monte Carlo simulation

To date, several computational phantoms have been proposed to represent WM, but most of them represent healthy brain tissues [29–34], thus, some of their features do not match those obtained from histology of pathological tissue. In the last decade, some efforts have been made to realize synthetic models of brain tissue in the presence of some specific pathological conditions, e.g. axons with bulges, crimps, and breakages in the computational framework of RWS (Random Walk simulator Software) by Landman et al. in [32], axonal bending by Budde and Frank [35], or axonal undulation by Nilsson et al. [37].

Regarding pathological processes involved in MS, in 2017, Salan et al. [36] proposed a synthetic phantom

encompassing spherical and diamond-shaped glial cells and myelinated axons with impermeable boundaries to approach, for the first time, the effects that demyelination has on the DTI parameters. The authors reported an increase in the DTI-derived Radial Diffusivity and Mean Diffusivity and a decrease in the Fractional Anisotropy. However, these results reflect the effects of only one structural change involved in the demyelination, i.e. the different configuration of the barriers. In particular, in this model, the myelin compartment is not different from the others in terms of relaxation time T2, whereas myelin has a very short T2 compared to the other tissues and, consequently, given the same volume, its contribution to the signal is relatively much smaller. As a consequence, their estimation of the signal change due to demyelination is likely larger than should be expected.

Here, we present an alternative WM model featuring, for the first time, myelinated axons with permeable membranes in the presence of demyelination and axonal loss. All the aforementioned works approaching the damaged conditions of WM, as well as the studies on DWI method validations using computational phantoms (e.g. [14, 18]), rely on impermeable compartments. However, the effect of the cell membrane permeability and the water exchange rate between compartments on the diffusion signal is non-negligible when using sequences with diffusion times greater than 12 ms in the case of a healthy brain, and 4 ms in injured conditions [38]: the typical sequences used in clinical studies to perform DTI, DKI, or NODDI analysis have diffusion times on the order of 30–40 ms.

Specifically, we implemented a Monte Carlo simulation of the diffusion motion of synthetic water molecules (called walkers for brevity) inside a synthetic environment (called substrate), containing several parallel non-abutting myelinated axons, each of them being represented by a pair of coaxial cylinders: the inner one representing the axon, and the space between the inner and the outer cylinders representing the myelin. The outer radii are distributed according to the gamma-function below:

$$P(x; k, \theta) = \frac{x^{k-1} e^{-x/\theta}}{\Gamma(k)\theta^k}, \quad (1)$$

with scale parameter $\theta = 2.493 \times 10^{-7}$ m and shape parameter $k = 2.877$. Hall et al. [31] obtained these values by fitting a gamma distribution to one of the histograms of axon radii reported by Aboitiz et al. in a histological study on the body section of the corpus callosum (CC) [54]. The ratio between the inner and the outer radius, i.e. the g -ratio, is fixed for all axons and set equal to $g\text{-ratio}_h = 0.7$ in healthy conditions, since histological studies report that g -ratio values are relatively constant and close to 0.7, in both the healthy human CC and macaque CC [55, 56]. We neglected the further confounding effect of dispersion in fiber orientation since this

study focuses on evaluating the effects of the demyelination and axonal loss on the diffusion-weighted MR signal.

In this simulation study, we modeled the myelin sheath as a compartment limited by two boundaries: the inner membrane, separating axon and myelin, and the external membrane separating the myelin from the outer space. We did not model any further structure inside this compartment but, rather, address the physical characterization of it by considering its whole volume (changing with demyelination degree), by calculating the cumulative probability of crossing the boundaries (Appendix B), and by directly taking into account the measurements, in the real myelin, of the apparent diffusivities (Appendix A) and the relaxation time (Appendix C). On the other hand, modeling the myelin sheath as a wound oligodendrocyte membrane would have been exceedingly complex and would have required the knowledge of the effective permeability of the wound oligodendrocyte membrane (different from that of a simple membrane). These data, to our knowledge, are not available in the literature, whereas available data on apparent diffusivities and relaxation time consist of values on the whole myelin sheath, averaged over the voxel or specimen.

In any case, our method consists of calculating the diffusion-weighted signal generated by a synthetic tissue that mimics a real one and comparing the information about the tissue extracted from this signal (e.g. fractional volumes of the compartments) using a specific diffusion method, with the ground truth values of the same synthetic tissue. Our idea was that taking into account the main aspects of the real myelin, as well as of the other compartments, that influence the diffusion signal, our modeling simplifications would not have overly affected the reliability of the results. In detail, all three compartments of the environment, i.e. the intra-axonal, the intra-myelin, and the extra-cellular space, are characterized by specific spatial diffusivities, boundary permeabilities, and T2 relaxation times.

Concerning the spatial diffusivities, we considered that the intrinsic diffusion motion is free throughout the substrate, and set the same diffusion coefficient $D_{\text{int}}(\text{sim}) = 2.02 \times 10^{-9} \text{ m}^2/\text{s}$, in the intra-axonal and extra-cellular spaces, in healthy conditions, adopting the choice of the authors of Camino and RWS [30–32] (both of which including only these two compartments). Given the intrinsic diffusivity of free liquid water at 310 K (body temperature) is $D_{\text{free}} = 3.0 \times 10^{-9} \text{ m}^2/\text{s}$, the lower value $D_{\text{int}}(\text{sim})$ should compensate for the effect of the hindrance of the several organelles and proteins not modeled in the synthetic environment. Regarding the intra-myelin space, we also set the value of its intrinsic diffusivity equal to $D_{\text{int}}(\text{sim})$ in the intra-myelin space, assuming that the substantial differences between the directional apparent diffusion coefficients measured in the real myelin [57] and the intrinsic diffusion coefficient

in the intra-axonal space and in the extracellular space, is mainly due to the presence of the barriers (cell membranes) rather than to an actual difference between the intrinsic diffusivities. We show in Appendix A that such an assumption is plausible.

Regarding the boundary permeability, we characterized differently the axonal and myelin membranes. For the axonal membranes, we relied on the values of water membrane permeabilities for the neurons reported by Boss et al. in a mice cell culture experiment [58] and on the measurements of permeability of axons reported by Stanisz [59] conducting a diffusion study on a sample of optic bovine nerve. For the myelin, we modeled a permeable membrane the crossing probability of which decays exponentially with myelin thickness. We used the findings on the real trends of the DTI-derived parameters, with increasing demyelination and axonal loss in the real tissues, as a reference for our simulation, to appropriately set the parameters characterizing the membrane permeabilities. We found that, when simulating the myelin sheath as totally impermeable or weakly permeable, the trends of AD and RD obtained in the simulation with increasing g -ratio do not match with those reported in the literature [60–63]. Appendix B describes our method to implement the permeability of the boundaries, considering the results on DTI parameters in the literature.

Concerning the T2 relaxation times in the different compartments, we relied on the values measured by Whittall et al. in [64]: the authors reported a T2 value of 15 ms for the intra-myelin space of CC and a mean T2 value of 78 ms in the WM. Accordingly, in the intra-myelin space, we set $T2_m = 15$ ms; in the intra-axonal and extra-cellular

space, we set $T2_o = 78$ ms. We used these T2 relaxation times to calculate the MR signal, by taking into account the time spent by each walker in each of the three compartments: more detail is given in Appendix C.

Finally, we modeled demyelination and axonal loss as two independent and superimposable processes, as reported in studies on neurodegenerative and demyelinating diseases [65–67]. Demyelination is modeled by leaving unchanged the distribution of the axonal inner radii and increasing the g -ratio, as well as, accordingly, the myelin transmission probability, as described in Appendix A. We modeled axonal loss by reducing the axonal density, while selectively eliminating axons with smaller radii, considering the experimental findings reported in post-mortem [66, 68], and in-vivo studies [65, 69–71] on MS lesions. Also, we took into account the effects on the extracellular diffusivity of the axonal debris, occurring as a consequence of axonal loss: Appendix D provides details of the implementation of the axonal loss and axonal debris processes.

Experimental design

We synthesized 21 substrates with different degrees of damage. Damage is characterized by the values of g -ratio and percentage of axonal loss p_{loss} . In one substrate we imposed the healthy conditions: g -ratio = 0.7 and $p_{\text{loss}} = 0$. In 10 substrates $p_{\text{loss}} = 0$ and g -ratio ranging from 0.71 to 0.97; in the others, g -ratio = 0.7 and p_{loss} ranging from 0.05 to 0.90 (Fig. 1). For each cubic substrate with $20 \mu\text{m}$ edge, the diffusion motion of 2×10^5 walkers were simulated for 6000 time-steps ($\delta t = 15.6 \mu\text{s}$). The MR signal was computed by

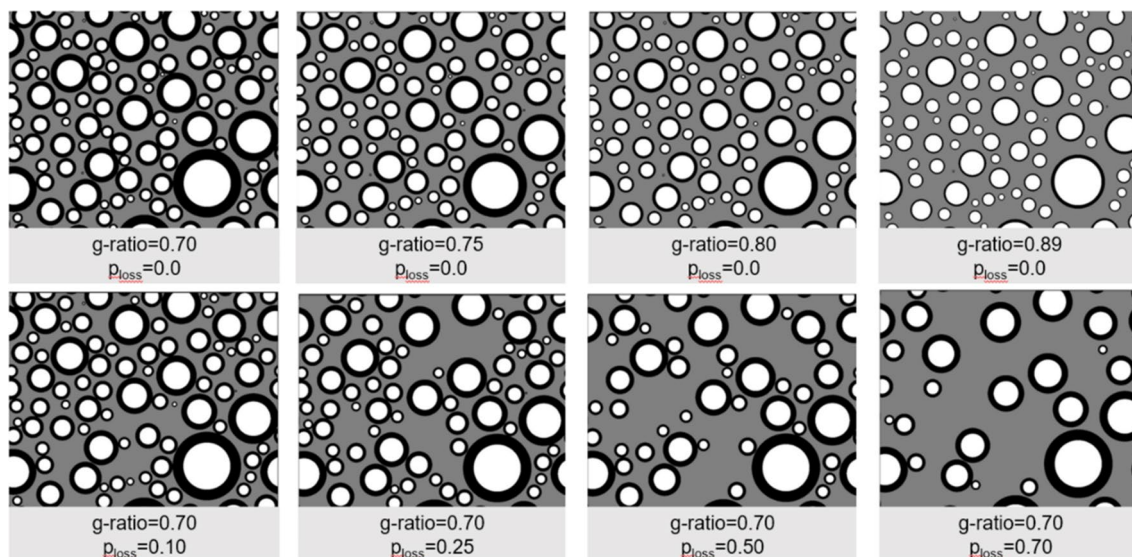


Fig. 1 Cross-sections of synthetic substrates with a fixed initial gamma distribution of radii ($\alpha = 2.877$, $\beta = 2.493 \times 10^{-7}$) and different degrees of damage in terms of g -ratio and p_{loss}

Table 1 Parameters of the acquisition protocols

Name of the sequence	N dir	b value (s/mm ²)	G (T/m)	Δ (s)	δ (s)	TE (s)	Approximated acquisition time (*) (min)
DTI	30	1000	0.0378	0.0387	0.0175	0.0780	8
2sh(a)	30	711	0.0318	0.0387	0.0175	0.0780	25
	60	2855	0.0638	0.0387	0.0175	0.0780	
2sh(b)	30	1000	0.0378	0.0387	0.0175	0.0780	17
	30	2000	0.0534	0.0387	0.0175	0.0780	
3sh(a)	6	300.2	0.0207	0.0387	0.0175	0.0780	14
	15	712.9	0.0319	0.0387	0.0175	0.0780	
3sh(b)	30	1997.8	0.0534	0.0387	0.0175	0.0780	
	30	1000	0.0378	0.0387	0.0175	0.0780	25
	30	2000	0.0534	0.0387	0.0175	0.0780	
5sh(a)	30	2855	0.0638	0.0387	0.0175	0.0780	
	6	300.2	0.0207	0.0387	0.0175	0.0780	25
	15	712.9	0.0319	0.0387	0.0175	0.0780	
DKI7sh	15	1301	0.0431	0.0387	0.0175	0.0780	
	30	1997.8	0.0534	0.0387	0.0175	0.0780	
	25	2855	0.0638	0.0387	0.0175	0.0780	
	30	400	0.0250	0.0350	0.0175	0.0700	59
	30	800	0.0353	0.0350	0.0175	0.0700	
	30	1200	0.0433	0.0350	0.0175	0.0700	
	30	1600	0.0500	0.0350	0.0175	0.0700	
NODDI5sh(b)	30	2000	0.0559	0.0350	0.0175	0.0700	
	30	2400	0.0612	0.0350	0.0175	0.0700	
	30	2800	0.0661	0.0350	0.0175	0.0700	
	6	300.2	0.0207	0.0387	0.0175	0.0780	27
	15	712.9	0.0319	0.0387	0.0175	0.0780	
	20	1997.8	0.0534	0.0387	0.0175	0.0780	
	25	2855	0.0638	0.0387	0.0175	0.0780	
	30	5302	0.0870	0.0387	0.0175	0.0780	

(*)The approximated acquisition time is calculated by considering that acquiring a whole-brain scan with 2 mm isotropic resolution along 90 different directions requires about 25 min [14]

using several Stejskal Tanner sequences the details of which are reported in Table 1; we superimposed a Rician noise with SNR = 20.

We evaluated the sensitivity to demyelination and axonal loss of each DWI parameter by performing the one-way analysis of variance (ANOVA). In detail, we determined whether there were any statistically significant differences between the means of the parameters (dependent variables) calculated in the healthy condition (g -ratio = 0.7, $p_{\text{loss}} = 0.0$) and in different conditions of g -ratio or p_{loss} (independent variables): significant differences were accepted at $p < 0.01$. Then, we carried out the post hoc Tukey test on the data to get a deeper insight into comparisons between the parameter means. In particular, for each parameter, damage process, and acquisition sequence, we used the Tukey test to compare each pair of means related to different degrees of damage to find out if they were significantly different or similar: again, significant differences were accepted at $p < 0.01$.

Statistical analysis was performed by means of MATLAB® (MathWorks, Natick, MA, USA). To summarize the statistical results, we used the Fisher test statistic F as an index of sensitivity for each damage process. Here, F corresponds to the ratio of the variance between the signal attenuations arising from different substrates (with different degrees of damage), and the variance of the attenuations within the single substrate. Greater F statistics reflect better results of the post hoc Tukey test, i.e. greater ability in distinguishing different degrees of damage, and thus, greater sensitivity.

DTI acquisition protocols and parameters

To date, the DWI technique most commonly used in the standard clinical practice is DTI [9–12], which assumes that diffusion motion is characterized by a Gaussian displacement distribution with a proper “apparent” diffusion coefficient (ADC) for each spatial direction. In detail, the shape

of the isosurface of the displacement probability density of water molecules is an ellipsoid and the eigenvalues λ_1 , λ_2 , λ_3 of the diffusion tensor represent the ADC along the principal axes of the ellipsoid [11]. DTI parameters, i.e. axial diffusivity (AD), radial diffusivity (RD), mean diffusivity (MD), and fractional anisotropy (FA), are combinations of the eigenvalues according to the formulas in [11] that summarize the diffusion properties of tissues and their degree of anisotropy; they have shown higher sensitivity to tissue structural changes in several pathological processes, as compared to the usual anatomic MRI techniques [72].

We selected, for DTI, an acquisition protocol typically employed in the clinical practice, consisting of 30 acquisitions along non-aligned directions uniformly distributed in space with b value = 1000 s/mm². Empirical evidence suggests this b value is the best choice for DTI analysis [73]. We derived the eigenvalues of the diffusion tensor through Camino [30] using weighted linear least-squares.

DKI acquisition protocol and parameters

In 2010, Jensen et al. [13] proposed the diffusional kurtosis imaging (DKI) that, regarding the diffusion motion of the water, quantifies the deviation of the displacement distribution from a Gaussian. DKI parameters are calculated along with the various spatial directions, according to formulas in [13]: in detail, considering a frame of reference that diagonalizes the diffusion tensor, the axial kurtosis AK is the diffusional kurtosis along the direction parallel to the largest diffusion eigenvalue (often referred to as parallel direction); the radial kurtosis RK is the diffusional kurtosis averaged over all directions perpendicular to the parallel one; the mean kurtosis MK is the diffusional kurtosis averaged over all directions. Finally, the fractional kurtosis KFA was proposed later, in 2015 [74], to provide a characterization of the kurtosis tensor without contributions from the diffusion tensor.

DKI parameters are found to be sensitive to the changes in the complexity of the tissue ascribed, for example, to the reactive astrogliosis [75], and axonal loss [76]. However, the exact meaning of the DKI parameters is still under debate and more studies are required to further validate the emerging data and to link changes in DKI parameters to pathologic findings.

DKI analyses are usually performed employing several acquisition protocols differing in the number of shells, gradient strength, and the number of diffusion gradient directions [39–42, 75–77]. The acquisition protocol consisting of two shells with 30 non-aligned directions and b values of 1000 and 2000s/mm² is commonly used in human studies, even if there are no agreed-upon guidelines in this respect. We used for our simulations six acquisition protocols for DKI, according to the empirical evidence indicating b values of

about 2000 – 3000s/mm² as an appropriate maximum and considering that 21 is the minimum number of non-aligned diffusion gradient directions given the DKI degrees of freedom [13, 78]. The protocol DKI7sh (see Table 1) consists of seven shells with 30 non-aligned directions and is often used in DWI studies on animal models [42]. Such a long acquisition time (> 60min) makes this sequence unsuitable for the standard clinical practice, however, it is informative, in this context, on the presumed highest sensitivity to damage provided by DKI parameters. The other sequences are the same as those used for NODDI, the maximum b value of which is less than 3000 s/mm²: this choice supports a possible unique acquisition protocol to perform the analysis of DW signals by means of more DWI methods, without losing too much in terms of parameter sensitivity.

DKI analysis is performed with the DKE software tool [79], using weighted linear least-squares, and implementing the physical and biological constraints described in [78].

NODDI acquisition protocols and parameters

Multi-compartmental DWI methods [14, 16–18] were developed to more accurately infer the microstructural properties of the tissue. These methods require high magnetic field gradient strengths (140–300 mT/m) and more demanding 3D q-space acquisition compared to DTI and DKI to discriminate between the hindered and restricted components of the model of diffusion (the acquisition time is on the order of 1 h or more). To date, the only compartmental method devised to be used with the low gradient strengths available on the common clinical MR scanners is NODDI (Neurite Orientation Dispersion and Density Imaging), proposed by Zhang et al. [14]. NODDI decomposed the observed diffusion signal as originating from three compartments. The intracellular (ic) compartment is the space bounded by the membrane of neurites, modeled as zero-radius cylinders, the orientation dispersion of which follows the Watson distribution: the diffusion motion occurs only along the axonal axial direction and is fully restricted perpendicular to them. The Orientation Dispersion Index, defined as OD in [14] and called ODI in [47], measures the orientation dispersion of the axons and ranges from 0 (for the parallel fibers) to 1 (for fully dispersed fibers). The extracellular (ec) space surrounds the axons and, also, is characterized by anisotropic and hindered diffusion; the isotropic (iso) space represents the cerebrospinal fluid CSF where the diffusion is isotropic and free. DW signal attenuation A_i coming from each compartment i contributes to the total DW signal attenuation A as follows [14]:

$$A = (1 - v_{\text{iso}})(v_{\text{ic}}A_{\text{ic}} + (1 - v_{\text{ic}})A_{\text{ec}}) + v_{\text{iso}}A_{\text{iso}}, \quad (2)$$

A_{iso} , A_{ic} , and A_{ec} are the signal attenuations related to, respectively, the isotropic compartment, the intra-cellular space, and the extra-cellular space; v_{iso} is the fraction of the whole voxel occupied by the isotropic compartment, while v_{ic} is the intra-cellular volume fraction of the part of voxel where diffusion is not isotropic.

$$\text{NDI} = (1 - v_{\text{iso}})v_{\text{ic}}, \quad (3)$$

NDI is the Neurite Density Index, i.e. the volume fraction of the voxel occupied by the intra-cellular space. NODDI parameters gave superior contrast compared to DTI parameters in demarking MS lesions [23, 44–48] and other neurodegenerative pathologies (e.g. Alzheimer’s disease [52]), stroke [51], and structural brain development [49, 50, 53].

For NODDI analysis, we selected six acquisition protocols. The protocols 2sh(a) and 3sh(a) (see Table 1) consist of, respectively, two and three shells and correspond to the protocols suggested by the authors of NODDI to achieve the best balance between the acquisition time (respectively ~30 min and 15 min) and accuracy of the parameters related to volume fractions [14]. The protocol 2sh(a) is recommended when high accuracy is required in measurements of axonal orientation dispersion. Despite the authors’ suggestions, many different acquisition protocols with two, and up to six shells, have been used to perform NODDI analysis on both healthy and lesioned tissue [47–53]. In 2014, Wang et al. [80] suggested that NODDI results obtained with a two-shell protocol and b values of 1000 and 2000s/mm² are comparable to those relying on the optimized protocol 3sh(a). The authors based this deduction on the comparison between the histograms of the parameter values throughout the brain of one healthy volunteer. Some studies performing NODDI analysis used this protocol [52, 53]. Given the purpose of this study, the acquisition protocol proposed by Wang et al. was included in the simulation as 2sh(b). We designed three additional protocols to better test the impact of the number of shells and diffusion gradient directions, and of higher values of the magnetic field gradient strength. In detail, one shell with 30 directions with b value = 2855s/mm² was added to 2sh(b) to obtain 3sh(b) and two five-shell protocols were obtained by adding two shells to the optimized protocol 3sh(a) using two different maximum magnetic field gradient strength: $G=0.0638$ T/m in 5sh(a); $G=0.087$ T/m in NODDI5sh(b). The upper limit of 96 diffusion gradient directions was respected for all the sequences to ensure a maximum acquisition time of ~30 min, feasible in the clinical practice. See Table 1 for a summary of protocol features.

We used the NODDI toolbox for Matlab (MATLAB®, MathWorks, Natick, MA, USA) [81] to compute the orientation dispersion index ODI, the isotropic volume fraction v_{iso} and v_{ic} ; finally, we calculated the neurite density

index NDI as in Eq. 3. We set the intra-cellular diffusivity for the NODDI method equal to $d_{\text{||}} = 1.7 \times 10^{-3}$ mm²/s, i.e. the value suggested by the authors of NODDI in [14] and reported as the optimum value to use in clinical studies (Guerrero et al. in [82]). Note that the diffusivity $d_{\text{||}}$ is not directly comparable to the value of the intrinsic diffusivity $D_{\text{int}}(\text{sim})$ set in the simulation, and it is not solely linked to the intrinsic diffusivity characterizing the real intra-axonal space, but it also compensates for the simplification of NODDI in describing the axons as non-myelinated sticks.

Results

Figures 2, 3, 4, 5 and 6 show the Monte Carlo simulation results on the DTI, DKI, and NODDI parameters calculated in different conditions of demyelination or axonal loss. As Sect. “Experimental design” explained, for each DWI parameter, damage process, and acquisition sequence, we performed the one-way ANOVA analysis to test if the parameter is sensitive or not to the damage process; then, we performed the post hoc Tukey test to evaluate how sensitive the parameter is to the degree of damage. We used the Fisher test statistic F as an index of sensitivity to summarize the results of the statistical analysis since greater F reflects better results of the post hoc Tukey test and, consequently, greater sensitivity. Tables 2 and 3 report, for each acquisition sequence, the F test statistics for the parameters that showed statistically significant changes between healthy and damaged condition (one-way ANOVA with $p < 0.01$). Concerning Table 3, please note that we did not use all the sequences for both the DKI and NODDI analyses. In particular, the sequence NODDI5sh(b) involves too high a gradient for the DKI analysis; also, the sequence DKI7sh is too long to be feasible in the standard clinical practice, thus, its use in the NODDI analysis is outside the scope of this study.

Due to demyelination, DTI-derived AD and MD do not significantly change with g -ratio; RD increases and FA decreases when g -ratio increases. With the increasing axonal loss, RD and MD increase, whereas FA and AD decrease.

Figure 3 shows the variation in the DKI-derived parameters induced by increasing the percentage of axonal loss, in the case of significant changes ($p < 0.01$) between the parameters calculated in the healthy and damaged conditions. On the other hand, in most cases DKI parameter did not vary significantly due to demyelination. The first result is that the acquisition protocol has an influence on the parameter sensitivity to the damage. The best sensitivities are obtained with a five-, rather than a seven-shell sequence (Table 3) and, in any case, they are comparable to, or lower than, the sensitivities of DTI parameters. Finally, the parameter averages can significantly vary across protocols as well, e.g. KFA in Fig. 3b.

Concerning NODDI, the acquisition protocol strongly impacts the parameter sensitivity to the damage and on the parameter mean values. The largest differences in terms of both sensitivity and mean values occur between the results obtained with five-shell sequences and those obtained with two- and three-shell sequences; additional minor differences, but still non-negligible, exist between the results of the optimized protocols 2sh(a) and 3sh(a), and those of 2sh(b) and 3sh(b). The best sensitivities are achieved by NDI and ν_{iso} with 2sh(a) and 3sh(a) (see Table 3 and Figs. 4 and 5). Generally, with two- or three-shell sequences, these parameters show high sensitivity to demyelination and excellent sensitivity to axonal loss. The parameters ν_{ic} and ODI are not sensitive to demyelination and scarcely sensitive to axonal loss except for severe cases (see Table 3 and Fig. 6).

Discussion

This diffusion simulation explored the specific effects that demyelination and axonal loss have on the DKI- and NODDI-derived parameters, using seven different diffusion sampling schemes (Figs. 3, 4, 5 and 6). We evaluated, for the first time, the impact of the acquisition protocol on the sensitivity of these parameters to the demyelination and axonal loss, with the goal of identifying a biomarker for demyelinating diseases to be used in the clinical practice. For this purpose, we developed a new model of synthetic WM tissue that includes some novelty elements never considered in the previous simulation studies, e.g. the boundary permeability and a myelin compartment with a specific T2 relaxation time.

We calculated the DW signal coming from the tissue with different degrees of damage, employing various acquisition protocols. For each DWI method and acquisition sequence, we extracted the output parameter and quantified their sensitivities to the damage processes by using the F-test statistic. We selected typical clinical acquisition protocols from the literature and designed some others ad hoc by limiting the maximum number of acquisitions to 96 and the maximum magnetic field gradient to values obtainable in a standard 3 T scanner (63.8mT/m and 87mT/m).

The DTI results presented in the literature about parameter trends in the presence of demyelination and axonal loss [60–63, 83–88], were used to calibrate the boundary permeability parameters.

We found that, when simulating the myelin sheath as being totally impermeable or weakly permeable, the trends of AD and RD obtained in the simulation with increasing g-ratio did not match with those reported in the literature [60–63]. Instead, we achieved consistent results by

modeling the axonal membrane as a permeable membrane with a physiologically realistic permeability [58], and the myelin sheath with a crossing probability exponentially decaying with myelin thickness.

We will now review the results of the simulation of DKI and NODDI parameters using clinically feasible DWI acquisition protocols, showing that they allow the detection of axonal loss and demyelination. We will also see that the ability to detect minute changes in the lesioned tissue depends on the acquisition protocol in an unexpected way: for example, increasing the number of shells or acquisitions does not necessarily translate into a higher sensitivity to damage.

DKI findings

The observed decrease of the mean kurtosis MK and increase of the axial kurtosis AK with increasing the percentage of axonal loss is consistent with the findings of many studies on MS patients [23, 39, 40] reporting lower values of MK and higher values of AK in lesions compared to healthy tissue. Concerning the trends of the DKI parameters in the case of demyelination, we found that DKI parameters are non-sensitive to demyelination with the exception of MK for protocol 5sh(a). On the other hand, an increase of MK, RK, and AK was reported by Guglielmetti et al. [42] in the CC of a cuprizone mouse model in the presence of demyelination, and severe inflammation, using a seven-shell sequence. However, the authors hypothesized the observed increment in DKI parameters was due to the high level of microgliosis present in the tissue and not to the demyelination process. Indeed, higher cellularity translates into an increase in the microstructural complexity, as reported in studies examining brain tumors where high-grade gliomas were compared to low-grade gliomas [43].

In addition to the specific effects of demyelination and axonal loss on the DKI parameters, the major finding of our simulation relates to the strong influence that the acquisition protocol has on the DKI parameter mean values and, especially, on their sensitivity to the damage.

In 2017, Chuhutin et al. [19] conducted a diffusion study on synthetic and experimental data (in-vivo human brain and ex-vivo rat brain) and reported that mean kurtosis MK strongly depends on both the experimental b-value and tissue type. In 2018, in a diffusion study on ex-vivo specimens of mice [20], Hutchinson et al. similarly found that DKI parameters were highly vulnerable to the effects of DWI sampling scheme: this dependence may differentially influence DKI parameters depending on the tissue type or even the axes along which the excess kurtosis is calculated. In both studies, the dependence of the DKI parameters on the diffusion sampling was ascribed to their dependence on

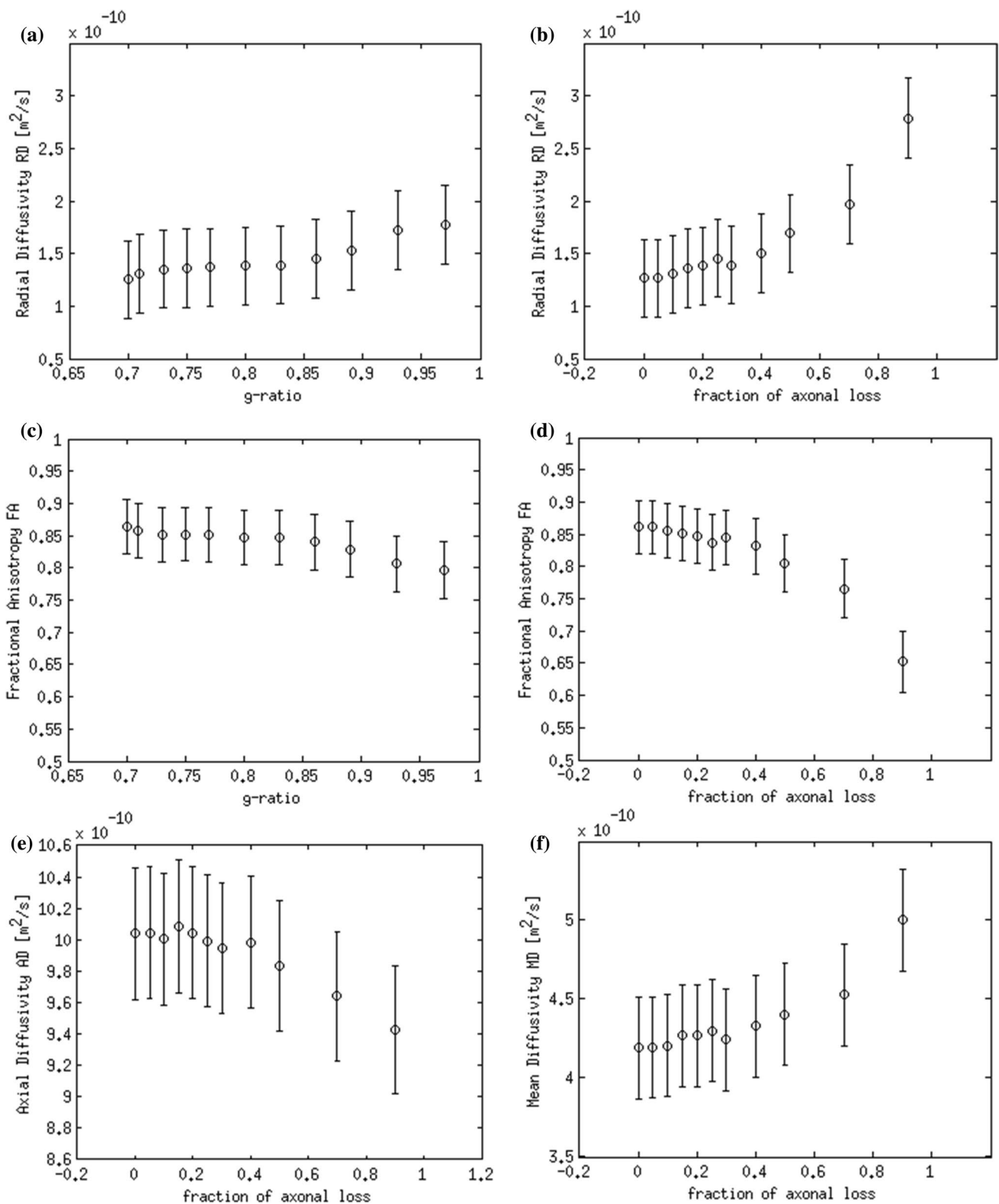


Fig. 2 Results of the Monte Carlo simulations for DTI parameters expressed in terms of mean and standard deviation, considering a Rician noise with SNR=20 affects the synthetic DW signal. In **a** and **b**, radial diffusivity RD values with increasing *g*-ratio and fraction of axonal loss p_{loss} , respectively; in **c** and **d**, fractional anisotropy

FA values with increasing *g*-ratio and fraction of axonal loss, respectively; in **e** and **f**, axial diffusivity AD and mean diffusivity MD values with increasing fraction of axonal loss. Changes in AD and MD induced by increasing *g*-ratio are omitted because not significant ($p > 0.01$)

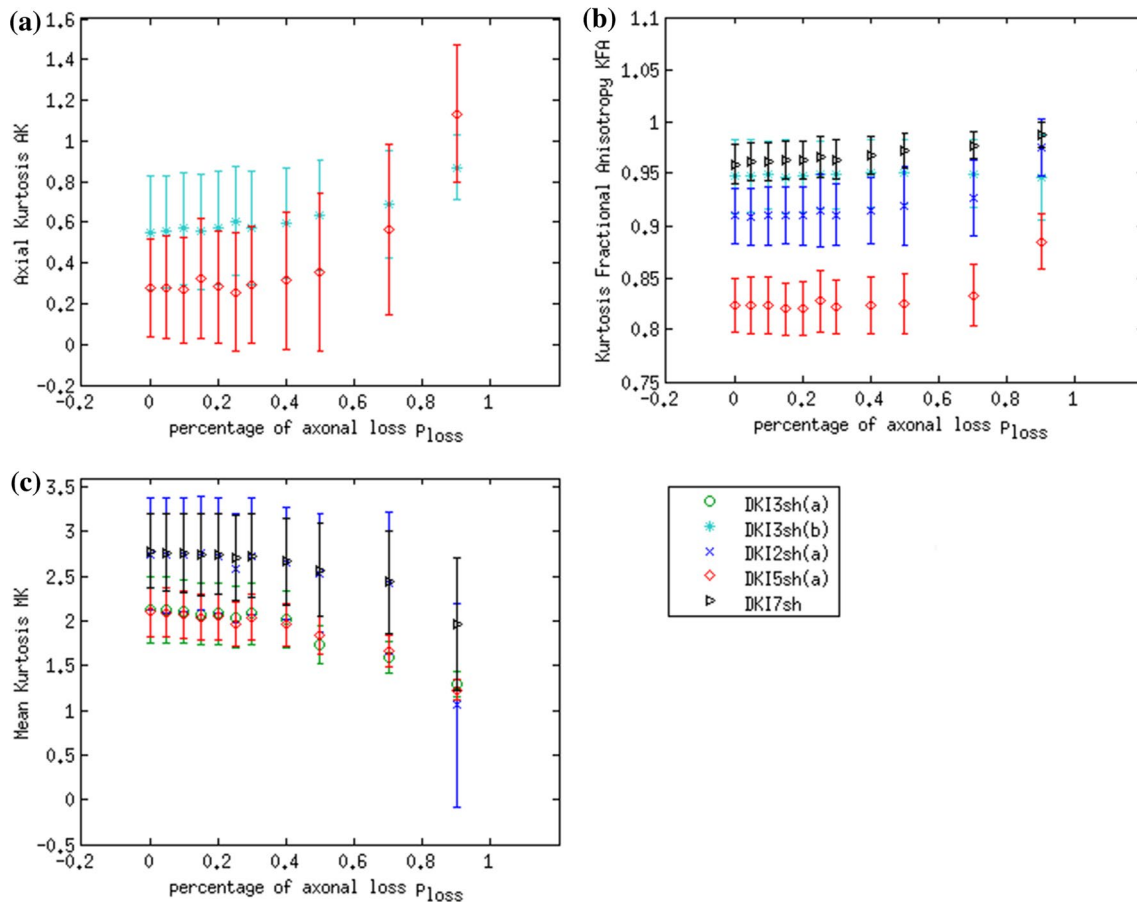


Fig. 3 Results of the Monte Carlo simulations for DKI parameters showing significant changes with increasing axonal loss ($p < 0.01$): in **a**, **b**, and **c**, the changes induced in AK, KFA, and MK respectively. Results are expressed in terms of mean and standard deviation, con-

sidering a Rician noise with $SNR = 20$ affects the synthetic DW signal. In most cases, DKI parameters did not significantly change with increasing demyelination

b -value: indeed, DKI parameters are calculated by considering the expansion of the logarithm of signal attenuation to the 4th-order DKI model, which is quadratic in b value. On the other hand, the dependence of the parameter mean values on the tissue type could be due to the discrepancy between the DKI model of the signal and the actual signal: such discrepancy changes with the microstructural features of the tissue (e.g. degree of anisotropy). In this context, our finding of the dependence on the acquisition protocol of the parameter sensitivity to the damage could stem from the influence of both b -values and tissue type on the DKI parameters, as found in the above studies. In detail, sensitivity to damage depends on the variation of a parameter in different conditions of damage, namely in tissues with different microstructural features, that, differently influence the parameters, depending on b value.

Another interesting result of our investigation is that we obtained the best sensitivities to damage not using a seven-shell sequence, but rather with a two-, three-, or five-shell sequence. This is contrary to the common assumption in the literature, according to which the greater the number of the shells and diffusion gradient directions, the better the sensitivity to the damage of the DWI parameters, irrespective of the DWI method used. However, for DKI, using more data does not always bring better results, and this is likely caused by the complex influence of the acquisition protocol and tissue type on the parameters, as discussed above.

Given the strong influence of the acquisition protocol on DKI parameters and particularly on the sensitivity to damage, as found in our simulation, comparing experimental results of DKI analysis, relying on different acquisition sequences, could lead to erroneous conclusions regarding the presence or severity of the damage. Further investigations

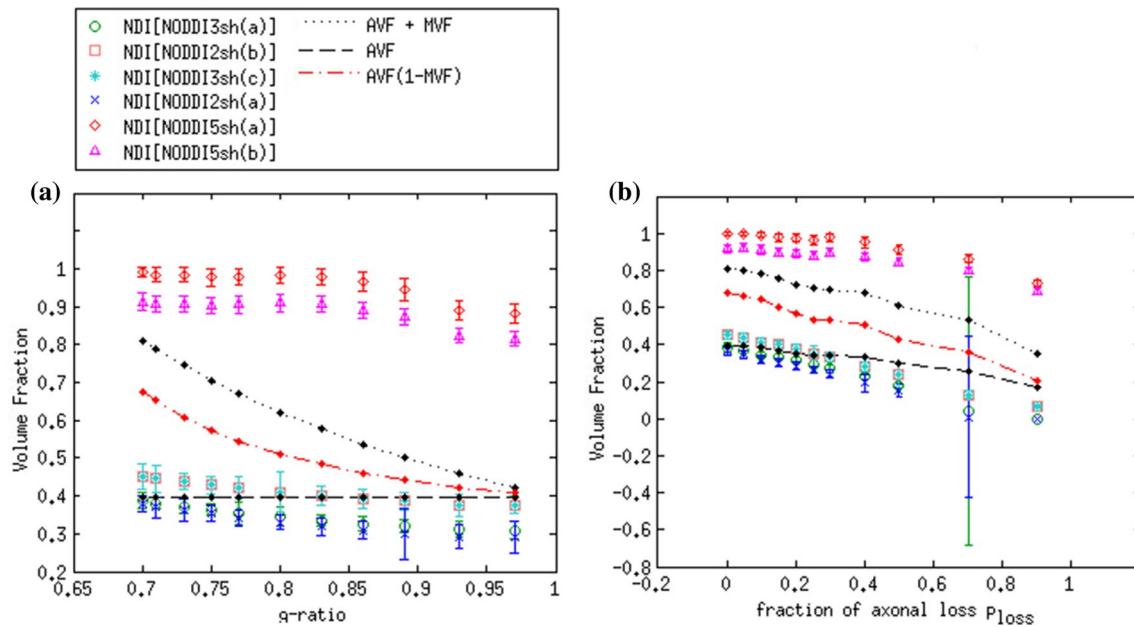


Fig.4 Results of the Monte Carlo simulations for NODDI parameter Neurite Density Index NDI (i.e. the NODDI-derived intra-cellular fractional volume), using 6 different acquisition protocols. In a and b, NDI mean values and standard deviations were obtained in different conditions of demyelination and axonal loss, respectively, consider-

are needed to find a community consensus on acquisition details.

NODDI findings: parameter sensitivity to the damage

For NODDI parameters our simulation study alerts about the even more evident difference between the results obtained using different acquisition sequences since the difference concerns both the parameter sensitivity to the damage and the parameter absolute values. For each acquisition protocol, NDI can reveal different degrees of both axonal loss and demyelination with the best sensitivity among all the NODDI-derived parameters; however, the optimal results across the sequences have been achieved when using the protocols optimized for NODDI by the authors of the method, i.e. 2sh(a) and 3sh(a) (Table 3 reports the F-test statistic, used as an index of sensitivity, across the parameters, damage processes, and sequences). The sensitivity of NDI to the myelin content has already emerged in an MRI-histological study conducted by Grussu et al. [47] on several post-mortem human MS and HC spinal cord specimens.

ing a Rician noise with SNR = 20 affects the synthetic DW signal. For reference, some specific combinations of the true intra-axonal fractional volume AVF and true intra-myelin fractional volume MVF are also shown

The authors ascribed this finding to both the effect that the altered membrane permeability has on NDI [87, 88], and to the fact that even if myelin water were virtually invisible in diffusion MRI due to its very short T2 [89], when myelin is lost, the local T2 increases, effectively increasing the amount of water with longer T2 and causing NDI to decrease [90].

It is also interesting to note that DKI parameter sensitivities obtained with the sequences optimized for NODDI by the authors of the method (i.e. 2sh(a) and 3sh(a)) and with the sequence 5sh(a) (obtained by adding two shells to 3sh(a)) are very good compared to the others used in this study and this suggests the possibility of using a single specific acquisition sequence to perform DWI analysis with both DKI and NODDI methods, without compromising parameter sensitivities. In this regard, By et al. [23] conducted a diffusion study on MS patients by using 2sh(a) and performing both NODDI and DKI analysis on the cervical spinal cord: NDI, ODI, MK, AK, and RK turned out to be effectively sensitive to the damage.

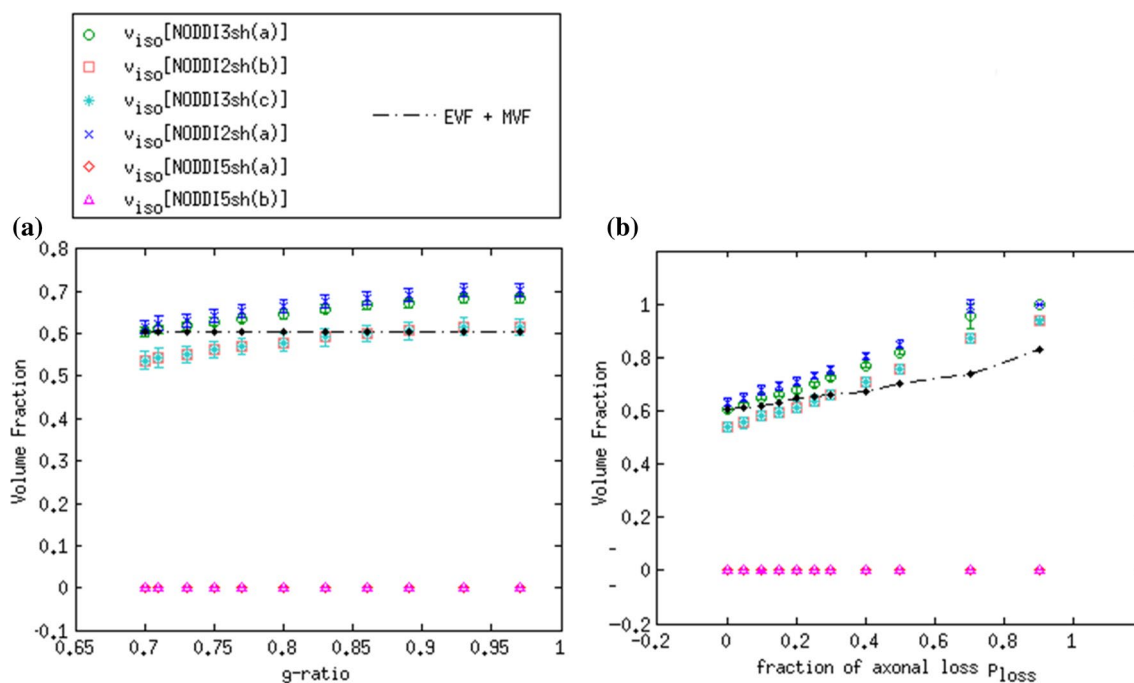


Fig. 5 Results of the Monte Carlo simulations for NODDI parameter Isotropic Volume Fraction v_{iso} , using 6 different acquisition protocols. In **a** and **b**, v_{iso} mean values and standard deviations obtained in different conditions of demyelination and axonal loss, respectively, con-

sidering a Rician noise with $SNR=20$ affects the synthetic DW signal. For reference, the sum of the extra-cellular volume fraction EVF and intra-myelin volume fraction MVF is also shown

NODDI findings: parameter absolute values

Moreover, our simulations allow comparing the values of the NODDI parameters, with some microstructural features of the synthetic substrate.

Concerning ODI, since the synthetic axons are parallel, it should be zero and remain unchanged with increasing demyelination or axonal loss. Overall, ODI values are close to zero, but bad trends occur in the presence of severe axonal loss when using two-shells protocols or less than 90 diffusion gradient directions: an impairment in method accuracy translates to high ODI values.

Regarding fractional volume estimations, in general, the absolute values of the parameters obtained with a five-shell sequence are very different from those obtained with two or three shells. In particular, with five-shell protocols, NDI is greater than the sum of the intra-axonal and intra-myelin space. On the other hand, with two- and three-shell sequences, NDI estimates the true intra-axonal volume fraction with good accuracy (slightly worsening with damage due to its dependence on the myelin content): this finding makes this parameter a potential biomarker of the true intra-axonal volume fraction (Fig. 4). Concerning v_{iso} , it attempts to measure the fractional volume characterized by isotropic diffusion (CSF): here its true value is zero. Figure 5 shows that, with five-shell sequences, v_{iso} values have zero mean,

Table 2 F test statistic of the changes in the DTI parameters induced by demyelination (variable g -ratio) and axonal loss (variable percentage of axonal loss p_{loss})

	MD	AD	RD	FA
g -ratio	–	–	4.05	5.09
p_{loss}	4.75	10.69	29.30	41.19

Omitted results refer to parameters showing non-significant changes between healthy and damaged condition (one-way ANOVA with $p < 0.01$)

in the presence of both demyelination and axonal loss; with two- or three-shell sequences, v_{iso} is very close to the true fractional volume consisting of the extra-cellular and intra-myelin space, at least in the case of non-severe damage. Finally, v_{ic} should be exactly equal to NDI (Eq. 3 with $v_{iso} = 0$) but this is verified only when using five-shell sequences (Fig. 6).

A similar strong dependence of NODDI results across acquisition protocols with different numbers of shells and diffusion gradient directions and strength emerged in the diffusion study on a fixed mouse brain conducted by Hutchinson et al. [20] (mentioned in the discussion on the DKI findings), and, also, in a very recent in-vivo study conducted by Li et al. in 2019, on a single healthy adult macaque monkey [22]. Furthermore, the aforementioned MRI-histological study conducted by Grussu et al. [47], reported high values

Table 3 *F*-test statistic of the changes in the DKI and NODDI parameters induced by demyelination (variable *g*-ratio) and axonal loss (variable percentage of axonal loss p_{loss})

		2sh(a)	2sh(b)	3sh(a)	3sh(b)	5sh(a)	NODDI5sh(b)	DKI7sh
AK	<i>g</i> -ratio	–	–	–	–	–	NC	–
	p_{loss}	–	–	–	0.07	13.85	NC	–
MK	<i>g</i> -ratio	–	–	–	–	3.19	NC	–
	p_{loss}	9.68	–	15.62	–	23.88	NC	4.57
KFA	<i>g</i> -ratio	–	–	–	–	–	NC	–
	p_{loss}	7.91	–	9.30	–	–	NC	4.56
NDI	<i>g</i> -ratio	79.28	39.42	178.29	39.42	61.96	53.37	NC
	p_{loss}	1325.33	895.20	1258.81	895.20	277.91	219.55	NC
v_{iso}	<i>g</i> -ratio	72.67	41.99	159.96	41.99	–	–	NC
	p_{loss}	1406.98	970.37	1359.07	970.37	–	–	NC
v_{ic}	<i>g</i> -ratio	–	–	–	–	61.96	53.37	NC
	p_{loss}	331.89	6.43	83.58	6.43	277.92	220.54	NC
ODI	<i>g</i> -ratio	–	–	–	–	36.04	44.48	NC
	p_{loss}	346.07	53.26	86.01	53.26	168.68	210.42	NC

Parameters axial kurtosis AK, mean kurtosis MK, radial kurtosis RK, and kurtosis fractional anisotropy KFA are DKI-derived, while neurite density index NDI, fractional volume v_{iso} of the compartment with isotropic diffusion, fractional volume v_{ic} of the intra-cellular space, and orientation dispersion index ODI are NODDI-derived

omitted results (–) refer to parameters showing non-significant changes between healthy and damaged condition (one-way ANOVA with $p < 0.01$). NC means Not Calculated, since not all the sequences were used for both the DKI and NODDI analyses

of NDI (ranging from 0.5 up to 1.0) with ground truth values of the intra-axonal fractional volume lower than 0.4 when using a sequence with six shells, *b* values ranging from 520 to 18,720 s/mm², and 121 isotopically distributed diffusion gradient directions: these outcomes fully support our results in the case of using five shells.

In short, it appears that it is not feasible to estimate, at the same time, all the true intra-cellular, extra-cellular, and CSF fractional volumes with good accuracy with NODDI due to its simplified model of the microstructure lacking the myelin compartment. Up to three shells, NODDI models the signal coming from the intra-axonal space of the substrate as coming from the intra-cellular space. It models the rest of the signal mainly as coming from CSF, failing to identify in the substrate the extra-cellular space ($v_{\text{ic}} \sim 1$ for two- and three-shell protocols in Fig. 6a, b). In the case of five shells, the greater complexity of the data allows NODDI to rule out CSF (which is not present in the substrate), but then the signal is modeled as coming mostly from the intra-cellular compartment.

On one hand, it would be interesting to further investigate the NODDI parameters when using diffusion sampling schemes with two and three shells in real tissues where also the CSF and cells are present: these structures, not modeled in our simulation, are characterized by an isotropic diffusion, thus, there is a good chance that NDI will estimate the true intra-axonal volume still with good accuracy and,

if so, NDI would be a very useful biomarker for the true neurite density. On the other hand, as an alternative and more pragmatic clinical approach, NDI could be viewed as a biomarker without considering its relation to the true intra-axonal fractional volume, and, consequently, the objective of standardizing the protocol would not be to improve the estimation accuracy, but rather to optimize the sensitivity to a given pathology.

Contribution of the myelin to the MR signal

In our simulation study, myelin is not completely invisible to the diffusion MR signal, as previous studies presumed due to very short T2 [55, 89]. In detail, Stikov et al. in a combined histologic and diffusion study [55] investigating on the myelin, found out the relationship between the NODDI-derived NDI and the true intra-myelin volume fraction MVF and true intra-axonal volume fraction AVF of the tissue, supposing that myelin does not contribute to the diffusion MR signal:

$$\text{NDI} = \text{AVF}/(1 - \text{MVF}). \quad (4)$$

However, our simulation results showed that, whatever the diffusion sampling scheme is used, the above Eq. 4 does not hold. Figure 4a, b report the comparison between the NDI results, and the quantity $\text{AVF}/(1 - \text{MVF})$ (in red), given the true MVF and AVF of the synthetic tissues.

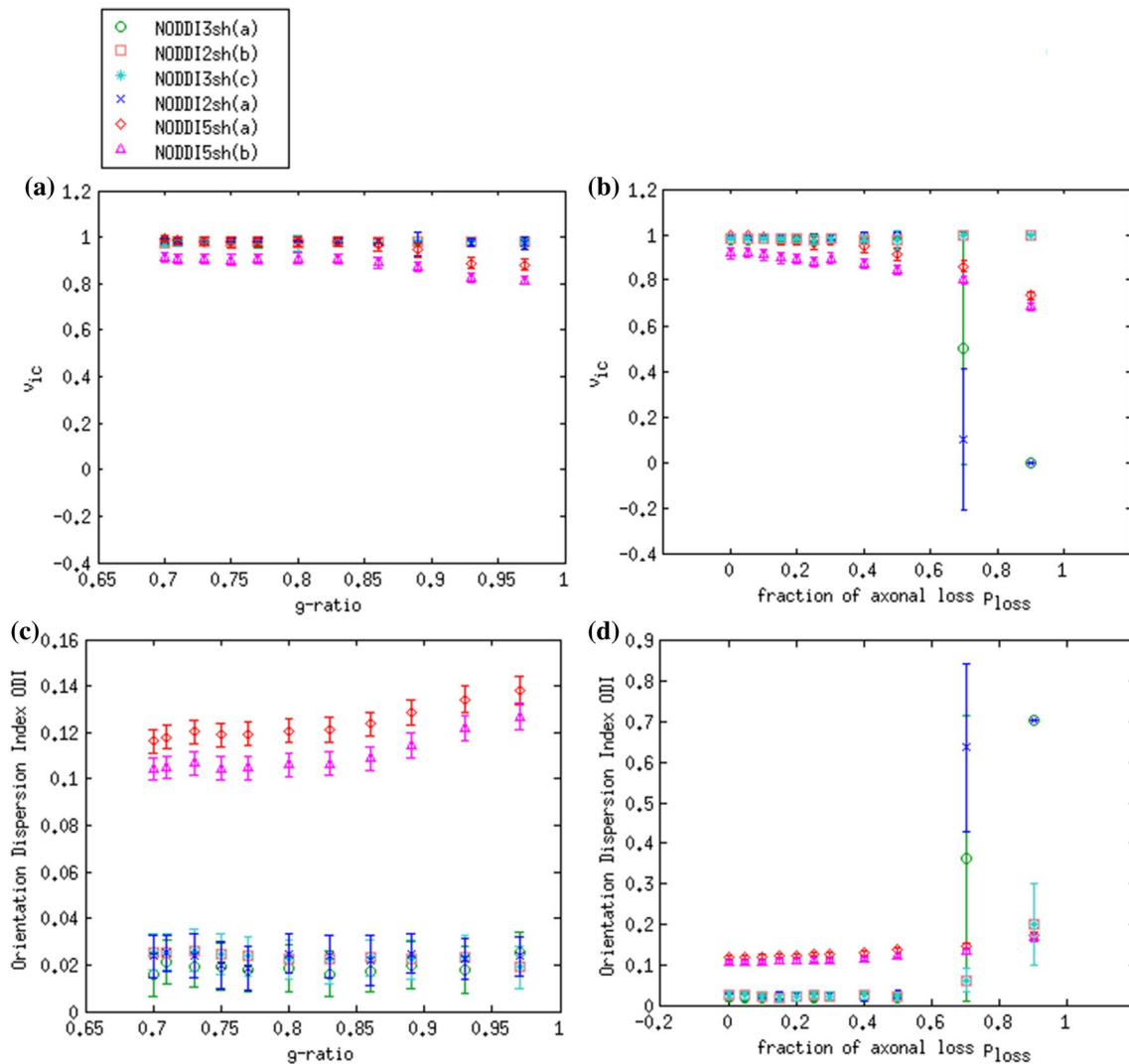


Fig. 6 Results of the Monte Carlo simulations for NODDI parameters by using 6 different acquisition protocols. Results are expressed in terms of mean and standard deviation, considering a Rician noise with SNR=20 affects the synthetic DW signal. In **a** and **b**, the

changes induced in the fraction of non-isotropic volume occupied by intra-cellular space ν_{ic} by demyelination and axonal loss, respectively. In **c** and **d**, the changes induced in the Orientation Dispersion Index ODI by demyelination and axonal loss, respectively

Concerning this relationship, it should be noted that the diffusion MRI – histological study by Grussu et al. [47] (mentioned above, in the discussion on NODDI findings) did not report equality between NDI and $AVF/(1 - MVF)$ but only correlation.

Conclusion

In conclusion, this study explored the feasibility of using Monte Carlo simulations of diffusion in synthetic tissues to assess which WM structural changes induced by specific damage processes underlying neurodegenerative and, particularly, demyelinating diseases, DWI parameters can actually detect when using clinically feasible acquisition protocols. In this regard, we demonstrated, for the first time,

that the effects of the boundary permeability, as well as the contribution of the myelin compartment to the MR signal, are not negligible, especially when simulating damage processes involving changes in these features.

In detail, we employed two DWI methods that are widely used to characterize lesioned tissues in the patients with demyelinating disease, i.e. DKI and NODDI, and compared them to DTI, in their ability in revealing the damage. We demonstrated that the results of the diffusion analysis relying on these methods can dramatically change when using different acquisition protocols. This finding points out the need to standardize the sequences, in view of a better interpretation of the parameter changes, and towards a correct comparison of the experimental results of diffusion studies.

Certainly, the model of synthetic WM presented here represents a simplification of the real WM tissue since, for example, it lacks microglia, and dispersion in the orientations of the axons is not considered. However, the differences in the parameter sensitivities, and, in the case of NODDI, in the parameter absolute values obtained by using different acquisition protocols cannot be ascribed to such limits of our synthetic WM model. Thus, further investigations in vivo would be appropriate to confirm these findings.

In following up this work, we would like to increase the complexity of the model geometry, by introducing spherical compartments representing the astrocytes and the dispersion in the orientation of the fibers. On the other hand, it could be advantageous to model other kinds of damage processes like microgliosis and edema. Also, these types of simulations could be useful in approaching the DWI analyses that involve more complex DWI compartmental methods as CHARMED, AxCaliber, and ACTIVEAX, requiring high gradient strength (140–300mT/m) and long acquisition time (at least 1 h), given their many degrees of freedom.

Author contributions DGC: supervision, drafting of the manuscript and critical revision. OS: study conception and design, acquisition of data, analysis and interpretation of data and drafting of the manuscript. All authors read and approved the final manuscript.

Compliance with ethical standards

Conflict of interest The authors declare that they have no conflict of interest.

Appendix A: Intrinsic diffusivity in the intra-myelin space

In our synthetic model of WM, we set a priori the value of water intrinsic diffusivity, into the synthetic myelin, equal to the value set for the other compartments i.e. $D_{\text{int}}(\text{sim}) = 2.02 \times 10^{-9} \text{m}^2/\text{s}$, since there are no suitable measurements of the intrinsic diffusivity of water in the real myelin. Thus, in this Appendix, we will evaluate the plausibility of our hypothesis by comparing the apparent diffusivity calculated along the radial direction in the synthetic myelin, with the apparent diffusivity measured along the radial direction in the real myelin. In detail, Andrews et al. conducted an ex-vivo study on the excised frog sciatic nerve and measured the directional apparent diffusion coefficients in the intra-myelin space [57], reporting $\text{ADC}_{\text{m}\parallel} = 3.7 \times 10^{-10} \text{m}^2/\text{s}$ and $\text{ADC}_{\text{m}\perp} = 1.3 \times 10^{-10} \text{m}^2/\text{s}$ along, respectively, the axial and the radial direction of the axon. In our simulation, by setting the intrinsic diffusivity in the intra-myelin space equal to $D_{\text{int}}(\text{sim}) = 2.02 \times 10^{-9} \text{m}^2/\text{s}$, we obtained $\text{ADC}_{\text{m}\parallel}(\text{sim}) = 0.7 \times 10^{-10} \text{m}^2/\text{s}$ and

$\text{ADC}_{\text{m}\perp}(\text{sim}) = 0.06 \times 10^{-10} \text{m}^2/\text{s}$; the synthetic myelinated fibers range in radius between 0.07–2.5 μm , with an average radius equal to 0.7 μm . Given that the frog sciatic nerve contains myelinated fibers ranging in radius between 0.5–10 μm [91], we have to consider, at least, the differences in terms of fiber radius, to compare the directional apparent diffusivities in the myelin obtained in this simulation with those reported by Andrews et al. [57]. In the case of Brownian motion, i.e. diffusion motion in the absence of a concentration gradient, the average distance l a water molecule diffuses during the time Δ is $l = \sqrt{2D\Delta}$ [7]. In the intra-myelin space of a given axon A_1 , along the radial direction, we can approximate the average distance l with half the difference between the outer R_1 and the inner radius r_1 of A_1 , following the same procedure used by Stanisiz et al. in [59]:

$$l = \frac{R_1 - r_1}{2} = \frac{R_1(1 - g)}{2}, \quad (5)$$

where g is the g -ratio = 0.7 in the healthy condition. Thus, the ratio of the apparent diffusion coefficients $\text{ADC}_{\text{m}\perp}$ in the intra-myelin space, along the radial direction, of two axons A_1 and A_2 with outer radii R_1 and R_2 , is:

$$\frac{\text{ADC}_{\text{m}\perp 1}}{\text{ADC}_{\text{m}\perp 2}} = \frac{R_1^2}{R_2^2}, \quad (6)$$

There is no information about the average radius of the axons populating the specific sample analysed by Andrews et al. [57]. However, the typical distribution of the axonal radii of the frog sciatic nerve can be approximated with a Gamma function with a positive skewness [16], so we may presume that the average radius ranges from 0.5 to 5 μm , i.e., respectively, the inferior limit and midpoint of the radius interval [0.5–10 μm] reported in the literature for the sciatic frog nerve fibers [91]. By using Eq. 2 with $\text{ADC}_{\text{m}\perp 1} = 0.06 \times 10^{-10} \text{m}^2/\text{s}$, i.e. our estimated value of the radial intra-myelin ADC, $R_1 = 0.7 \mu\text{m}$, i.e. the average radius of the synthetic fibers, $\text{ADC}_{\text{m}\perp 2} = 1.3 \times 10^{-10} \text{m}^2/\text{s}$, i.e. the intra-myelin ADC measured ex-vivo in a frog sciatic nerve by Andrews et al. in [57], we obtain an average radius of the frog sciatic nerve fibers equal to $R_2 = 3.3 \mu\text{m}$, that is physically plausible ($0.5 \mu\text{m} < R_2 < 5 \mu\text{m}$).

Appendix B: Boundary permeabilities

The synthetic tissue of WM presented in this simulation study consists of three compartments, i.e. the intra-axonal space, the intra-myelin space, and the extra-cellular space. The boundaries separating the intra-axonal and the intra-myelin spaces, and those separating the intra-myelin and the extra-cellular spaces are permeable: we had to characterize

them considering that, to our knowledge, the only useful measurements of water permeability, reported in the literature, are affected by both the neuron membrane and myelin sheet.

In detail, when a walker encounters a membrane, it is either reflected or transmitted, with a membrane transmission probability P . P depends on the membrane biochemical characteristics translating to a permeability value k . To ensure no net flux across the membrane [32], the relation between k and P , from inside to outside and vice versa is:

$$P_{\text{in[out]} \rightarrow \text{out[in]}} = k / (1/4 \cdot v_{\text{in[out]}}), \quad (7)$$

where

$$v_{\text{in[out]}} = \sqrt{6D_{\text{in[out]}} / \delta t}, \quad (8)$$

v is the average speed of walkers, δt is the unit time-step, and D is the intrinsic diffusivity. In this simulation, v is obtained from Eq. 2, with $\delta t = 15.6 \mu\text{s}$ and $D = 2.02 \times 10^{-9} \text{m}^2/\text{s}$ as described in the section Materials and Methods; P is obtained from Eq. 1, given v and the permeability k , that is the only free parameter of the simulation strictly linked to the boundary characterization.

As described above, in our synthetic tissue there are two kinds of membranes to characterize: k_a and P_a relate to the membrane separating the axon from the myelin; k_{outer} and P_{outer} refer to the boundary separating the myelin from the extra-cellular space. Notably, in this simulation, P_{outer} represents the probability, for a water molecule, to cross the whole myelin sheet, thus, we set k_{outer} to obtain physically plausible values for P_{outer} .

Stanisz et al. conducted a study on the bovine optic nerve [59] and reported an overall value of $k_{a\text{-outer}(1)} = 0.9 \pm 0.2 \times 10^{-5} \text{m/s}$ for an axonal membrane encompassing the myelin sheath. We set $0.7 \times 10^{-5} \text{m/s}$ as the lower limit of k_a . Similarly, an overall value of $k_{a\text{-outer}(2)} = 4.7 \pm 3 \times 10^{-5} \text{m/s}$, was reported by Boss et al., in a cell culture study [58], as the water membrane permeability of the mice neurons: we set $5 \times 10^{-5} \text{m/s}$ as the upper limit of k_a . Initially, we set the values of k_a and k_{outer} equal for all the myelinated axons. We performed several simulation trials by setting k_a values in the range $[0.7 - 5.0] \times 10^{-5} \text{m/s}$, and $k_{\text{outer}} < k_a$, since the myelin sheath is presumably less permeable than a simple cell membrane. We evaluated the impact of P_a and P_{outer} on DW signal changes induced by increasing the g -ratio, to simulate demyelination, using a typical sequence for DTI analysis. We expected that, with a decrease in myelin, the bulk apparent diffusion coefficient (derived from DTI) along the axial direction AD should not significantly change, whereas the one along the radial direction RD should significantly

increase, as widely reported in DWI studies on shiverer mice CNS presenting demyelination but no axonal injury or inflammation [60–63]. On the contrary, in silico, when k_{outer} values are fixed to be equal for all the axons and lower than $0.7 \times 10^{-5} \text{m/s}$, an increase of g -ratio causes AD to decrease and RD to slightly decrease, albeit not significantly, regardless of the choice of k_a and the thickness of the myelin. This means that, if the myelin sheath is modeled as totally impermeable ($k_{\text{outer}} = 0 \text{m/s}$) or slightly permeable ($k_{\text{outer}} < 0.7 \times 10^{-5} \text{m/s}$), the trends of AD and RD obtained in simulation with increasing g -ratio do not match those reported in the literature [60–63].

We obtained the expected trends for AD and RD by modelling P_{outer} to exponentially decrease with myelin thickness and setting $k_a = 5 \times 10^{-5} \text{m/s}$ equal for all the axons. This kind of model for P_{outer} is conceived by considering that the true myelin sheath is a greatly extended plasma membrane of a glial cell (oligodendrocyte in WM) wrapped around the axon in a spiral fashion: therefore, a water molecule moves through it without being transported through aquaporins, crosses N cell membranes with a probability P_{outer} exponentially decreasing with myelin thickness:

$$P_{\text{outer}} = P_g^N, \text{ with } P_g = P_a, \quad (9)$$

where P_g is the membrane crossing probability of a glial cell: in this model we assume that P_g is the same as for the axonal membrane crossing probability P_a . To realize such a dependence of P_{outer} on the myelin thickness, we set k_{outer}^* for one particular axon A^* and obtained the relative value of P_{outer}^* from the Eq. 1. Then, we extracted the number N^* of membrane turns wrapping around A^* by using the Eq. 3. Finally, we calculated N^i , and then P_{outer}^i for all other axons A^i , by considering the ratio in myelin thickness between A^* and A^i .

After implementing the P_{outer} model, further simulation trials were performed by changing k_a in the range $[0.9 - 5] \times 10^{-5} \text{m/s}$. Lower k_a values determine AD decrements, and non-significant RD increments, when the g -ratio increases, hence we definitely set $k_a = 5 \times 10^{-5} \text{m/s}$.

Finally, k_{outer}^* was set to the value $1.5 \times 10^{-8} \text{m/s}$ to set a balance between its effects on the outer membrane permeability and the pre-exchange lifetime in myelin, which increase and decrease with increasing k_{outer}^* values, respectively.

Technically, the pre-exchange lifetime τ_m is the time required for 63% (e^{-1}) of the intra-cellular water to exchange [38]. In this regard, many studies conducted on animal models [92–94] have reported τ_m values in the range [43 – 150] ms, depending on the distribution of the axonal diameters: $\tau_m = 43 \text{ms}$ was measured by Harkins et al. [92]

in a rat spinal cord portion with a mean axonal radius of $(0.6 \mp 0.2) \mu\text{m}$ and a myelin volume fraction of 0.51. In our simulation, the mean axonal radius is $0.7 \mu\text{m}$, and the myelin volume fraction is 0.3, therefore, to compare the value of the pre-exchange lifetime in real myelin (as reported in [92]) with our simulation, we have to take at least into account the difference in myelin volume fraction since the mean axonal radii are very similar.

Considering the linear dependence between the pre-exchange lifetime in a given space and volume fraction of the same space [38], we expect the following relation:

$$\frac{\text{MVF}_r}{\text{MVF}_s} = \frac{\tau_r}{\tau_s}, \quad (10)$$

where MVF_r and τ_r , and MVF_s and τ_s , are, respectively, the myelin volume fraction and pre-exchange lifetime in real myelin and in simulation. From Eq. 4, given $\text{MVF}_r = 0.51$, $\text{MVF}_s = 0.3$ and $\tau_r = 43$ ms, we obtain $\tau_s = 25$ ms. In this simulation, given all the free parameters (diffusivity and permeabilities) set as discussed above, we obtained a pre-exchange lifetime in the synthetic myelin equal to $\tau_m = 10$ ms: this value is in the correct order of magnitude and is physically plausible, considering the different experimental conditions in which the histological ex-vivo values [92] were obtained.

Appendix C: MR diffusion signal

The signal loss for each walker is computed considering the total time Δt_a , Δt_m , Δt_{ec} spent during the TE, respectively, in the intra-axonal, intra-myelin, and extra-cellular space. Dephasing depends on the net displacement during the diffusion time Δ (assuming the short-pulse approximation). Ensemble effects are computed by integrating dephasing in time and summing over all the walkers:

$$\frac{S}{S_0} = \frac{\sum_{\text{walkers}} \cos \theta(\Delta) \cdot e^{-\left(\frac{\Delta t_a}{T_{2o}} + \frac{\Delta t_m}{T_{2m}} + \frac{\Delta t_{ec}}{T_{2o}}\right)}}{\sum_{\text{walkers}} e^{-\left(\frac{\Delta t_a}{T_{2o}} + \frac{\Delta t_m}{T_{2m}} + \frac{\Delta t_{ec}}{T_{2o}}\right)}} \quad \text{with } \Delta t_a + \Delta t_m + \Delta t_{ec} = \text{TE}, \quad (11)$$

$\cos \theta(\Delta)$ is the attenuation of the signal for one molecule in the case of a dephasing θ due to the net displacement during the diffusion time Δ ; T_{2o} is the T2 relaxation time in the intra-axonal and extra-cellular space, while T_{2m} relates to the intra-myelin compartment. In vivo [95] and in vitro [96] studies on the human brain and ex vivo studies on animal models [64, 96–99] support T2 in the range [10–20] ms for the myelin water. We set $T_{2m} = 15$ ms and $T_{2o} = 78$ ms, as Whittall et al. [64] measured, respectively, the intra-myelin space of CC and in the whole WM.

Appendix D: Implementation of the axonal loss and axonal debris processes

In neurodegenerative lesions, and in particular, in the demyelinating diseases, the major contribution to the axonal loss is given by the Wallerian Degeneration (WD) occurring when a nerve fiber is cut or crushed and the part of the axon farther from the neuron cell body degenerates [100–103]. Irrespective of the specific mechanism underlying axonal loss, the result is a decrease in axonal density together with the formation of axonal debris. As reported later, both these microstructural changes of tissue substantially affect water diffusion.

A decrease in axonal density is modeled considering an experimental observation reported in post-mortem [66, 68] and in-vivo studies [65, 69–71] on MS lesions: in all the analysed CNS areas, a selective death of axons with a smaller radius, roughly lower than $1 \mu\text{m}$, occurs in both acute and chronic lesions. Thus, a fraction p_{loss} of axonal loss translates to a random elimination of $p_{\text{loss}} \cdot N_h$ axons from their distribution in healthy conditions, with N_h the initial number of axons. Selective death of smaller axons is implemented by extracting the outer radii of the axons to be deleted from a sigmoidal distribution function with the inflection point at $1 \mu\text{m}$, and further selecting the axons with a radius smaller than $1 \mu\text{m}$, if still present in the substrate.

Regarding the axonal debris, histological studies [104, 105] described what happens immediately after the axonal degeneration. Widespread granular disintegration of axoplasmic microtubules and neurofilaments occurs in the 24–72-h interval following axonal degeneration. Amorphous granular breakdown products from nerve fibers progressively leave the intra-cellular space in 48 h and amorphous granular deposits of increasing prominence appear within the space around the axonal membranes of the lost axon. The presence of such deposits in the lesioned area have been still observed

30–34-days after nerve degeneration. In a one-year follow-up diffusion study of stroke patients, Yu et al. [106] reported at the second week a sharply decreased DTI-derived FA and AD, and increased RD; then, from the second week to the third month, MD slightly increased accompanied by a decrease in FA, an increase in RD, and no change in AD; finally, all diffusion indices remained at a relatively stable level after three months. The authors hypothesized that such changes of DTI indices might be ascribed to WD followed by the formation of axonal debris. In 2012, Qin et al. [105] conducted an in-vivo diffusion study combined with a

histological validation, on a pathological animal model (*felis catus*) presenting WD. Their results confirmed the trends for DTI indices and also the hypothesis of Yu et al. [106]. They found quick decreases in FA, and AD, and an increase in RD from the second day to the eighth day after axonal injury, which was accompanied by progressive axonal disintegration. Afterward, from the eighth day to the sixtieth day, a slow clearance of granular deposits of axonal debris within the space around the axonal membranes, caused FA, MD, and AD to slightly increase, while RD remained unchanged [105]. In detail, after 60 days, the AD value was found still 0.83 times lower than its value in a healthy condition. Another diffusion study on WD, by Thomalla et al. [107], reported an AD value, in the lesioned tissue, to be 0.86 times lower than its value in the healthy condition, 2 weeks after the damage.

Given all these findings we modeled axonal debris having in mind these considerations:

1. We hypothesized to scan the tissue when the amorphous granular deposits are in the extra-cellular space, around the axonal membrane of the lost axon, as mentioned before and observed in [104]. Thus, our model represents the lesioned tissue, at least 2 weeks after the axonal degeneration, when AD becomes relatively stable;
2. Since the granular deposits are similar to small organelles, the diffusion motion, occurring in the extra-cellular space in the presence of the amorphous granular deposits, may be considered as hindered (Gaussian-type);
3. Compared to a healthy condition, the presence of the granular deposits make AD and FA decrease, RD increase, and MD slightly increase;
4. Given the high and homogeneous density of the axons inside the substrate, in the healthy condition, we consider the extra-cellular space as approximately equally partitioned among the axons. Thus, for a given fraction p_{loss} of lost axons, we assume that a reduction in diffusivity, due to the presence of axonal debris, occurs in the same fraction p_{loss} of the extracellular space. Indeed, the axonal debris only affects the extracellular space closely surrounding each lost axon.

We modeled the presence of axonal debris in the extra-cellular space, by decreasing the diffusivity from $D = 2.02 \times 10^{-3} \text{ mm}^2/\text{s}$ (in the extra-cellular space in the healthy condition) to a lower value D_{debris} in a fractional volume of extra-cellular space equal to p_{loss} . Accordingly, the average diffusivity $\bar{D}(p_{\text{loss}})$ in the extra-cellular space is given by:

$$\bar{D}(p_{\text{loss}}) = p_{\text{loss}} \times D_{\text{debris}} + (1 - p_{\text{loss}}) \times D. \quad (12)$$

We evaluated the effect of different D_{debris} on the AD and RD trend when p_{loss} increases. We expected a significant AD decrement and RD increment with axonal loss, as reported in DWI studies on axonal injury [100–105]. If $D_{\text{debris}} = 0$, an increase in p_{loss} determines an increase in both AD and RD. Positive values of D_{debris} result in decreasing AD, and in a progressive reduction of the RD increment, with increasing p_{loss} . Further increase in the D_{debris} value leads to a point in which RD does not significantly change, and then decreases, with increasing p_{loss} . The expected AD and RD trends are obtained with approximately $D_{\text{debris}} = 1.8 \times 10^{-3} \text{ mm}^2/\text{s}$. Setting such a value implies that when axonal loss affects the whole substrate ($p_{\text{loss}} = 1$), $D(p_{\text{loss}}) = 0.89 D$, a physically plausible value, considering the results reported in the literature (in [107], AD value in the lesioned tissue was found to be 0.86 times lower than its value in the healthy condition). Figure 6 shows some examples of substrates with different degrees of demyelination and axonal loss.

References

1. Filippi M, Cercignani M, Inglese M, Horsfield MA, Comi G (2001) Diffusion tensor magnetic resonance imaging in multiple sclerosis. *Neurology* 56:304–311
2. Ito R, Melhem ER, Mori S, Eichler FS, Raymond GV, Moser HV (2001) Diffusion tensor brain MR imaging in X-linked cerebral adrenoleukodystrophy. *Neurology* 56:544–547
3. Maldjian JA, Grossman RI (2001) Future applications of DWI in MS. *J Neurol Sci* 186(Suppl 1):S55–S57
4. Nusbaum AO, Tang CY, Buchsbaum MS, Wei TC, Atlas SW (2001) Regional and global changes in cerebral diffusion with normal aging. *Am J Neuroradiol* 22(1):136–142
5. Roosendaal SD, Geurts JGG, Vrenken H et al (2009) Regional DTI differences in multiple sclerosis patients. *NeuroImage* 44:1397–1403
6. Metwalli NS, Benatar M, Nair G, Usher S, Hu X, Carew JD (2010) Utility of axial and radial diffusivity from diffusion tensor MRI as markers of neurodegeneration in amyotrophic lateral sclerosis. *Brain Res* 1348:156–164
7. Einstein E (1956) Investigations on the theory of the Brownian Movement. Dover Publications Inc, New York
8. Le Bihan D, Turner R (1991) Intravoxel incoherent motion imaging using spin echoes. *Magn Reson Med* 19:221–227
9. Tournier JD, Mori S, Leemans A (2011) Diffusion tensor imaging and beyond. *Magn Reson Med* 65:1532–1556
10. Mori S, Zhang J (2006) Principles of diffusion tensor primer imaging and its applications to basic neuroscience research. *Neuron* 51:527–539
11. Mori S (2007) Introduction to Diffusion Tensor Imaging. Elsevier Science
12. Beaulieu C (2002) The basis of anisotropic water diffusion in the nervous system - a technical review. *NMR Biomed* 15:435–455
13. Jensen JH, Helpern JA (2010) MRI Quantification of non-Gaussian water diffusion by kurtosis analysis. *NMR Biomed* 23(7):698–710
14. Zhang H, Schneider T, Wheeler-Kingshott CA, Alexander DC (2012) NODDI: practical in vivo neurite orientation dispersion and density imaging of the human brain. *NeuroImage* 61:1000–1016

15. Rovira A, Wattjes MP, Tintore M, Tur C, Yousry TA, Sormani MP et al (2015) MAGNIMS consensus guidelines on the use of MRI in multiple sclerosis—clinical implementation in the diagnostic process. *Nat Rev Neurol* 11:471–482
16. Assaf Y, Basser PJ (2005) Composite hindered and restricted model of diffusion (CHARMED) MR imaging of the human brain. *NeuroImage* 27:48–58
17. Assaf Y, Blumenfeld Katzir T, Yovel Y, Basser PJ (2008) AxCaliber: a method for measuring axon diameter distribution from diffusion MRI. *Magn Reson Med* 59:1347–1354
18. Zhang H, Hubbard PL, Parker GJM, Alexander DC (2011) Axon diameter mapping in the presence of orientation dispersion with diffusion MRI. *NeuroImage* 56:1301–1315
19. Chuhutin A, Hansen B, Jespersen SN (2017) Precision and accuracy of diffusion kurtosis estimation and the influence of b-value selection. *NMR Biomed* 30(11)
20. Hutchinson EB, Avram AV, Irfanoglu MO, Koay CG, Barnett AS, Komlosh ME, Ozarslan E, Schwerin SC, Juliano SL, Pierpaoli C (2018) Analysis of the effects of noise, DWI sampling, and value of assumed parameters in diffusion MRI models. *Magn Reson Med* 78:1767–1780
21. De Santis S, Assaf Y, Evans CJ, Jones DK (2014) Improved precision in CHARMED assessment of white matter through sampling scheme optimization and model parsimony testing. *Magn Reson Med* 71:661–671
22. Li CX, Patel S, Zhang X (2020) Evaluation of multi-shell diffusion MRI acquisition strategy on quantitative analysis using multi-compartment models. *Quant Imaging Med Surg* 10(4):824–834
23. By S, Xua J, Boxb BA, Bagnatoc FR, Smith SA (2017) Application and evaluation of NODDI in the cervical spinal cord of multiple sclerosis patients. *NeuroImage Clin* 15:333–342
24. De Santis S, Bastiani M, Droby A et al (2019) Characterizing microstructural tissue properties in multiple sclerosis with diffusion MRI at 7 T and 3 T: the impact of the experimental design. *Neuroscience* 403:17–26
25. Love S (2006) Demyelinating diseases. *J Clin Pathol* 59(11):1151–1159
26. Ellwardt E, Zipp F (2014) Molecular mechanisms linking neuroinflammation and neurodegeneration in MS. *Exp Neurol* 262:8–17
27. Weinshenker BG (1996) Epidemiology of multiple sclerosis. *Neurol Clin* 14:291–308
28. Dendrou CA, Fugger L, Friese MA (2015) Immunopathology of multiple sclerosis. *Nat Rev Immunol* 15:545–558
29. Balls GT, Frank LR (2009) A simulation environment for diffusion weighted MR experiments in complex media. *Magn Reson Med* 62:771–778
30. Cook A, Bai Y, Nedjati-Gilani S, Seunarine KK, Hall MG, Parker GJ et al (2006) Camino: open-source diffusion-MRI reconstruction and processing. *Proc Intl Soc Mag Reson Med* 14
31. Hall MG, Alexander DC (2009) Convergence and parameter choice for Monte-Carlo simulations of diffusion MRI. *IEEE Trans Med Imaging* 28:1354–1364
32. Landman BA, Farrell JAD, Smith SA, Reich DS, Calabresi PA, Van Zijl PCM (2010) Complex geometric models of diffusion and relaxation in healthy and damaged white matter. *NMR Biomed* 23:152–162
33. Yeh CH, Schmitt B, Le Bihan D, Li-Schlittgen JR, Lin CP, Poupon C (2013) Diffusion microscopic simulator: a general Monte Carlo simulation system for diffusion magnetic resonance imaging. *PLoS ONE* 8:e76626
34. Mingasson T, Duval T, Stikov N, Cohen-Adad J (2017) AxonPacking: an open-source software to simulate arrangements of axons in white matter. *Front Neuroinform* 11:5
35. Budde MD, Frank JA (2010) Neurite beading is sufficient to decrease the apparent diffusion coefficient after ischemic stroke. *Proc Natl Acad Sci USA* 107:14472–14477
36. Salan T, Jacobs EL, Reddick WE (2017) A 3D Model-based simulation of demyelination to understand its effects on diffusion tensor imaging. *Conf Proc IEEE Eng Med Biol Soc* 39
37. Nilsson M, Latt J, Stahlberg F, van Westen D, Hagslatt H (2012) The importance of axonal undulation in diffusion MR measurements: a Monte Carlo simulation study. *NMR Biomed* 25:795–805
38. Yang DM, Huettner JE, Bretthorst GL, Neil JJ, Garbow JR, Ackerman JJH (2017) Intracellular water preexchange lifetime in neurons and astrocytes. *Magn Reson Med* 79(3):1616–1627
39. Yoshida M, Hori M, Yokoyama K et al (2013) Diffusional kurtosis imaging of normal-appearing white matter in multiple sclerosis: preliminary clinical experience. *Jpn J Radiol* 31:50–55
40. Raz E, Bester M, Sigmund EE et al (2013) A better characterization of spinal cord damage in multiple sclerosis: a diffusional kurtosis imaging study. *Am J Neuroradiol* 34:1846–1852
41. Falangola MF, Guilfoyle DN, Tabesh A et al (2014) Histological correlation of diffusional kurtosis and white matter modeling metrics in cuprizone-induced corpus callosum demyelination. *NMR Biomed* 27:948–957
42. Guglielmetti C, Veraart J, Roelant E et al (2016) Diffusion kurtosis imaging probes cortical alterations and white matter pathology following cuprizone induced demyelination and spontaneous remyelination. *NeuroImage* 125:363–377
43. Raab P, Hattingen E, Franz K, Zanella FE, Lanfermann H (2010) Cerebral gliomas: diffusional kurtosis imaging analysis of microstructural differences. *Radiology* 254:876–881
44. Schneider T, Brownlee W, Zhang H, Ciccarelli O, Miller DH, Wheeler-Kingshott CAM (2014) Application of multi-shell NODDI in Multiple Sclerosis. *Proc Intl Soc Mag Reson Med* 22.
45. Granberg T, Fan Q, Treaba CA, Ouellette R, Herranz E, Mangat G et al (2017) In vivo characterization of cortical and white matter neuroaxonal pathology in early multiple sclerosis. *Brain* 140:2912–2926
46. Grussu F, Schneider T, Yates RL et al (2015) Histological metrics confirm microstructural characteristics of NODDI indices in multiple sclerosis spinal cord. ISMRM Meeting, Toronto Canada
47. Grussu F, Schneider T, Tur C, Yates RL et al (2017) Neurite dispersion: a new marker of multiple sclerosis spinal cord pathology? *Ann Clin Transl Neurol* 4(9):663–679
48. Collorone S, Cawley N, Grussu F, et al (2019) Reduced neurite density in the brain and cervical spinal cord in relapsing-remitting multiple sclerosis: a NODDI study. *Mult Scler* 1352458519885107
49. Bataille D, Hughes EJ, Zhang H, Tournier JD, Tumor N, Aljabara P et al (2017) Early development of structural networks and the impact of prematurity on brain connectivity. *NeuroImage* 149:379–392
50. Kodiweera C, Alexander AL, Harezlak J, McAllister TW, Wu Y (2016) Age effects and sex differences in human brain white matter of young to middle-aged adults: A DTI, NODDI, and q-space study. *NeuroImage* 128:180–192
51. Adluru G, Gur Y, Anderson JS, Richards LG, Adluru N, DiBella EVR (2014) Assessment of white matter microstructure in stroke patients using NODDI. *Conf Proc IEEE Eng Med Biol Soc* 742–745
52. Colgan N, Siowa B, O’Callaghan JM, Harrisona IF, Wells JA, Holmes HE et al (2016) Application of neurite orientation dispersion and density imaging (NODDI) to a tau pathology model of Alzheimer’s disease. *NeuroImage* 125:739–744
53. Jelescu IO, Veraart J, Adisetiyo V, Milla SS, Novikov DS, Fieremans E (2015) One diffusion acquisition and different white matter models: how does microstructure change in human

- early development based on WMTI and NODDI? *NeuroImage* 107:242–256
54. Aboitiz F, Scheibel AB, Fisher RS, Zaidel E (1992) Fiber composition of the human corpus callosum. *Brain Res* 598:143–153
 55. Stikov N, Campbell JSW, Stroh T, Lavelée M, Frey S, Novak J et al (2015) In vivo histology of the myelin g-ratio with magnetic resonance imaging. *NeuroImage* 118:397–405
 56. Berman S, West KL, Does MD, Yeatman JD, Mezer AA (2018) Evaluating g-ratio weighted changes in the corpus callosum as a function of age and sex. *NeuroImage* 182:304–313
 57. Andrews TJ, Osborne MT, Does MD (2006) Diffusion of Myelin Water. *Magn Reson Med* 56:381–385
 58. Boss D, Kühn J, Jourdain P, Depeursinge C, Magistretti PJ, Marquetta P (2013) Measurement of absolute cell volume, osmotic membrane water permeability, and refractive index of transmembrane water and solute flux by digital holographic microscopy. *J Biomed Opt* 18(3):036007
 59. Stanisz GJ, Szafer A, Wright GA, Henkelman RM (1997) An analytical model of restricted diffusion in bovine optic nerve. *Magn Reson Med* 37:103–111
 60. Song SK, Sun SS, Ramsbottom MJ, Chang C, Russell J, Cross AH (2002) Demyelination revealed through MRI as increased radial (but Unchanged Axial) diffusion of water. *NeuroImage* 17:1429–1436
 61. Song SK, Yoshino J, Le TQ et al (2005) Demyelination increases radial diffusivity in corpus callosum of mouse brain. *NeuroImage* 26:132–140
 62. Gulani V, Webb AG, Duncan ID, Lauterbur PC (2001) Apparent diffusion tensor measurements in myelin-deficient rat spinal cords. *Magn Reson Med* 45:191–195
 63. Aung WY, Mar S, Benzinger TLS (2013) Diffusion tensor MRI as a biomarker in axonal and myelin damage. *Imaging Med* 5(5):427–440
 64. Whittall KP, MacKay AL, Graeb DA, Nugent RA, Li DK, Paty DW (1997) In vivo measurement of T2 distributions and water contents in normal human brain. *Magn Reson Med* 37(1):34–43
 65. Kutzelnigg A, Lassmann H (2014) Pathology of multiple sclerosis and related inflammatory demyelinating diseases. In: Douglas J. Goodin, editors. *Multiple Sclerosis and related disorders*. Elsevier, vol 122 p 32
 66. Lassmann H (2010) Axonal and neuronal pathology in multiple sclerosis: what have we learnt from animal models. *Exp Neurol* 225:2–8
 67. De Luca GC, Williams K, Evangelou N, Ebers GC, Esiri MM (2006) The contribution of demyelination to axonal loss in multiple sclerosis. *Brain* 129:1507–1516
 68. Ganter P, Prince C, Esiri MM (1999) Spinal cord axonal loss in multiple sclerosis: a post-mortem study. *Neuropathol Appl Neurobiol* 25:459–467
 69. Bitsch A, Schuchardt J, Bunkowski S, Kuhlmann T, Bruck W (2000) Acute axonal injury in multiple sclerosis. Correlation with demyelination and inflammation. *Brain* 123:1174–1183
 70. Evangelou N, Konz D, Esiri MM, Smith S, Palace J, Matthews PM (2001) Size-selective neuronal changes in the anterior optic pathways suggest a differential susceptibility to injury in multiple sclerosis. *Brain* 124:1813–1820
 71. De Luca GC, Ebers GC, Esiri MM (2004) Axonal loss in multiple sclerosis: a pathological survey of the corticospinal and sensory tracts. *Brain* 127:1009–1018
 72. Jones DK, Knösche TR, Turner R (2013) White matter integrity, fiber count, and other fallacies. The do's and don'ts of diffusion MRI. *NeuroImage* 73:239–254
 73. Jones DK, Horsfield MA, Simmons A (1999) Optimal strategies for measuring diffusion in anisotropic systems by magnetic resonance imaging. *Magn Reson Med* 42:515–525
 74. Glenn GR, Helpert JA, Tabesh A, Jensen JH (2015) Quantitative assessment of diffusional kurtosis anisotropy. *NMR Biomed* 28(4):448–459
 75. Zhuo J, Xu S, Proctor JL et al (2012) Diffusion kurtosis as an in vivo imaging marker for reactive astrogliosis in traumatic brain injury. *NeuroImage* 59:467–477
 76. Steven AJ, Zhuo J, Melhem ER (2014) Diffusion kurtosis imaging: an emerging technique for evaluating the microstructural environment of the brain. *Am J Roentgenol* 202(1):W26–W33
 77. de Kouchkovsky I, Fieremans E, Fleysher L, Herbert J, Grossman RI, Inglese M (2016) Quantification of normal-appearing white matter tract integrity in multiple sclerosis: a diffusion kurtosis imaging study. *J Neurol* 263(6):1146–1155
 78. Tabesh T, Jensen JH, Ardekani BA, Helpert JA (2011) Estimation of tensors and tensor-derived measures in diffusional kurtosis imaging. *Magn Reson Med* 65:823–836
 79. <https://www.nitrc.org/projects/dke>
 80. Wang Z, Wang Y, Zhang J, Yan X, Liu H, Xiao Z (2014) The performance of NODDI estimation using a common 2-shell protocol. *Proc Intl Soc Magn Reson Med* 22
 81. <http://mig.cs.ucl.ac.uk/index.php?n=Tutorial.NODDIatlab>
 82. Guerrero JM, Adluru N, Bendlin BB et al (2019) Optimizing the intrinsic parallel diffusivity in NODDI: An extensive empirical evaluation. *PLoS ONE* 14(9):e0217118
 83. Song SK, Sun SW, Ju WK, Lin SJ, Cross AH, Neufeld AH (2003) Diffusion tensor imaging detects and differentiates axon and myelin degeneration in mouse optic nerve after retinal ischemia. *NeuroImage* 20:1714–1722
 84. Budde MD, Xie M, Cross AH, Song SK (2009) Axial diffusivity is the primary correlate of axonal injury in the experimental autoimmune encephalomyelitis spinal cord: a quantitative pixelwise analysis. *J Neurosci* 29:2805–2813
 85. Naismith T, Song SK, Cross AH, Benzinger TL (2011) Radial diffusivity predicts demyelination in ex vivo multiple sclerosis spinal cords. *NeuroImage* 55:1454–1460
 86. Wheeler-Kingshott CA, Cercignani M (2009) About “axial” and “radial” diffusivities. *Magn Reson Med* 61:1255–1260
 87. Shintaku M, Hirano A, Llena J (1988) Increased diameter of demyelinated axons in chronic multiple sclerosis of the spinal cord. *Neuropathol Appl Neurobiol* 14:505–510
 88. Lassmann H (2003) Axonal injury in multiple sclerosis. *J Neurol Neurosurg Psychiatry* 74:695–697
 89. Wu Y, Alexander AL, Fleming JO et al (2006) Myelin water fraction in human cervical spinal cord in vivo. *J Comput Assist Tomogr* 30:304–306
 90. Stevenson V, Parker G, Barker G et al (2000) Variations in T1 and T2 relaxation times of normal appearing white matter and lesions in multiple sclerosis. *J Neurol Sci* 178:81–87
 91. Wijesinghe RS, Gielen FL, Wikswo JP Jr (1991) A model for compound action potentials and currents in a nerve bundle. III: A comparison of the conduction velocity distributions calculated from compound action currents and potentials. *Ann Biomed Eng* 19(1):97–121
 92. Harkins KD, Dula AN, Does MD (2012) Effect of inter-compartmental water exchange on the apparent myelin water fraction in multiexponential T(2) measurements of rat spinal cord. *Magn Reson Med* 67(3):793–800
 93. Bjarnason TA, Vavasour IM, Chia CL, MacKay AL (2005) Characterization of the NMR behaviour of white matter in bovine brain. *Magn Reson Med* 54(5):1072–1081
 94. Stanisz G, Kecojevic A, Bronskill M, Henkelman R (1999) Characterizing white matter with magnetization transfer and T2. *Magn Reson Med* 42(6):1128–1136
 95. MacKay A, Whittall K, Adler J, Li D, Paty D, Graeb D (1994) In vivo visualization of myelin water in brain by magnetic resonance. *Magn Reson Med* 31(6):673–677

96. Fischer HW, Rinck PA, van Haverbeke Y, Muller RN (1990) Nuclear relaxation of human brain gray and white matter: analysis of field dependence and implications for MRI. *Magn Reson Med* 16:317–334
97. Menon RS, Rusinko MS, Allen PS (1992) Proton relaxation studies of water compartmentalization in a model neurological system. *Magn Reson Med* 28:264–274
98. Stewart WA, Mackay AL, Whittall KP, Moore GRW, Paty DW (1993) Spinspin relaxation in experimental allergic Encephalomyelitis. Analysis of CPMG data using a non-linear least squares method and linear inverse theory. *Magn Reson Med* 29:767–775
99. Mädler B, Drabycz SA, Kolind SH, Whittall KP, MacKay AL (2008) Is diffusion anisotropy an accurate monitor of myelination? Correlation of multicomponent T2 relaxation and diffusion tensor anisotropy in human brain. *Magn Reson Imag* 26:874–888
100. Ciccarelli O, Werring D, Barker G et al (2003) A study of the mechanisms of normal-appearing white matter damage in multiple sclerosis using diffusion tensor imaging. *J Neurol* 250:287–292
101. Dzedzic T, Metz I, Dallenga T, König FB, Müller S, Stadelmann C et al (2010) Wallerian degeneration: a major component of early axonal pathology in multiple sclerosis. *Brain Pathol* 20(5):976–985
102. Singh S, Dallenga T, Winkler A et al (2017) Relationship of acute axonal damage, Wallerian degeneration, and clinical disability in multiple sclerosis. *J Neuroinflamm* 14:57
103. Casanova B, Martínez-Bisbal M, Valero C et al (2003) Evidence of Wallerian degeneration in normal appearing white matter in the early stages of relapsing-remitting multiple sclerosis. *J Neurol* 250:22–28
104. Schlaepfer WW, Hasler MB (1979) The persistence and possible externalization of axonal debris during wallerian degeneration. *J Neuropathol Exp Neurol* 38(3):242–252
105. Qin W, Zhang M, Piao Y, Guo D, Zhu Z et al (2012) Wallerian Degeneration in central nervous system: dynamic associations between diffusion indices and their underlying pathology. *PLoS ONE* 7(7):e41441
106. Yu C, Zhu C, Zhang Y, Chen H, Qin W et al (2009) A longitudinal diffusion tensor imaging study on Wallerian degeneration of corticospinal tract after motor pathway stroke. *NeuroImage* 47:451–458
107. Thomalla G, Glauche V, Koch MA, Beaulieu C, Weiller C, Rothner J. (2004) Diffusion tensor imaging detects early Wallerian degeneration of the pyramidal tract after ischemic stroke. *NeuroImage* 22:1767–1774

Publisher's Note Springer Nature remains neutral with regard to jurisdictional claims in published maps and institutional affiliations.